JPL PUBLICATION 78-19

Application of Multispectral Radar and LANDSAT Imagery to Geologic Mapping in Death Valley

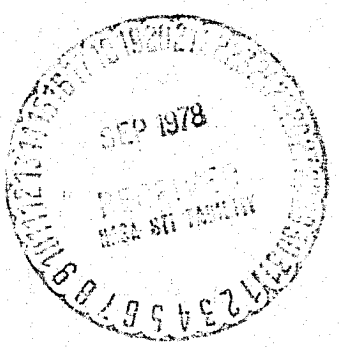

National Aeronautics and
Space Administration

Jet Propulsion Laboratory
California Institute of Technology
Pasadena, California

JPL PUBLICATION 78-19

Application of Multispectral Radar and LANDSAT Imagery to Geologic Mapping in Death Valley

M. Daily
C. Elachi
T. Farr
W. Stromberg
S. Williams
Jet Propulsion Laboratory

G. Schaber
U. S. Geological Survey
Flagstaff, Arizona

March 30, 1978

National Aeronautics and
Space Administration

Jet Propulsion Laboratory
California Institute of Technology
Pasadena, California

Prepared Under Contract No. NAS 7-100
National Aeronautics and Space Administration

Preface

The work described in this report was performed by the Telecommunications Science and Engineering Division of the Jet Propulsion Laboratory.

M. Daily is also with the Department of Geological Sciences at the University of California at Santa Barbara.

Acknowledgement

We thank the National Park Service for permission to collect samples in Death Valley National Monument and Mr. Pete Sanchez of the Monument staff for advice on various aspects of this work.

This report has benefitted from reviews by J. Ford, W. E. Brown, and A. Goetz.

Contents

Tables

Figures

Abstract

The purpose of this study was to apply the techniques of computer image processing to data sets from sensors operating in visible and microwave wavelengths as an aid to discriminating surficial geologic units.

Side-Looking Airborne Radar (SLAR) images acquired by JPL and Strategic Air Command systems and visible and near-infrared LANDSAT imagery were applied to studies of the Quaternary alluvial and evaporite deposits in Death Valley, California. Unprocessed radar imagery revealed considerable variation in microwave backscatter, generally correlated with surface roughness.

Individual images were registered to a common geographic base by first manually selecting an array of tiepoints and then geometrically distorting the images in a computer. The registered images were ratioed, picture element by picture element, then contrast-stretched to enhance the spectral differences.

For Death Valley, LANDSAT imagery is of limited value in discriminating the Quaternary units except for alluvial units distinguishable by presence or absence of desert varnish or evaporite units whose extremely rough surfaces are strongly shadowed.

In contrast, radar returns are most strongly dependent on surface roughness, a property more strongly correlated with surficial geology than is surface chemistry. While no single radar band is capable of separating all the surface units, use of two frequencies: (1) X-band, λ = 3 cm and (2) L-band, λ = 25 cm, and two polarizations: (1) vertical-transmit, vertical-receive (VV) and (2) vertical-transmit, horizontal-receive (VH) permits complete separation of all units except the two younger gravel units (Qg_3 and Qg_4 and the *enfant terrible* of the study, the floodplain (Qf). By including any one LANDSAT band, Qg_3 and Qg_4 become distinguishable, while Qf remains intractable.

Microwave scattering mechanisms in the Valley include specular reflection, diffuse (depolarizing), multiple scattering, and the effects of penetration.

Application of Multispectral Radar and LANDSAT Imagery to Geologic Mapping in Death Valley

I. Introduction

Remote sensing data at different wavelengths are being utilized in increasing amounts in synoptic geologic analysis of the Earth's surface as the appropriate sensor technology and analytical procedures are developed. A geologist uses remote sensing data as a tool for mapping structure and lithology. Structure mapping is greatly influenced by lighting geometry, by which lineaments and other topographic expressions of structure are observed. Additionally, good discrimination of lithology permits the identification of marker beds whose positions indicate folds, faults, and other structures. Rock-type discrimination is also essential for identifying likely sites for mineralization and fluid reservoirs and for determining the geologic history of an area. This report describes a multisensor approach to lithologic mapping.

We have examined the Quaternary geologic units of Death Valley, California, utilizing two sensor systems: visible and near-infrared imagery from LANDSAT and multifrequency/multipolarization radar data from JPL L-band and Goodyear X-band systems. We observe a dramatic synergistic effect among the data sets that demonstrates the usefulness of combining color information derived from visible/near infrared data with surface texture effects from multiconfiguration radar imagery. Geometric and photometric operations by computer image processing techniques prove to be the key to utilizing the full capabilities of such diverse sensors. The two basic sets of data, radar and LANDSAT, differ radically in image geometry. Additionally, there are substantial geometric differences between the L-band (JPL) and X-band (Goodyear) radar images. In order to perform comparative digital processing, it was necessary to identify a densely packed network of targets common to all images and to perform digital geometric corrections to create a family of LANDSAT and radar images, all of which are in precise registry. Images were generated by digital arithmetic operations (ratioing and differencing) on pairs of imagery. These composite images strongly accentuate differences between two sensors. Information from these ratio and difference images of three radar sensor configurations permits a nearly complete discrimination of the surface geologic units of Hunt and Mabey (1966). For the surficial geologic units present in Death Valley, the polarization anomaly images provide more information than do dual-frequency anomaly data. Use of the LANDSAT intensity image permits the discrimination of two alluvial fan gravel units that are not separated by the radar data. By color coding the dual-polarization L-band radar data and the LANDSAT intensity image, we have generated an unsupervised geologic map of Death Valley that exhibits reasonable correspondence with published geologic maps (Fig. 1).

Modern technology and atmospheric transmission properties permit the use of imaging sensors operating at wavelengths

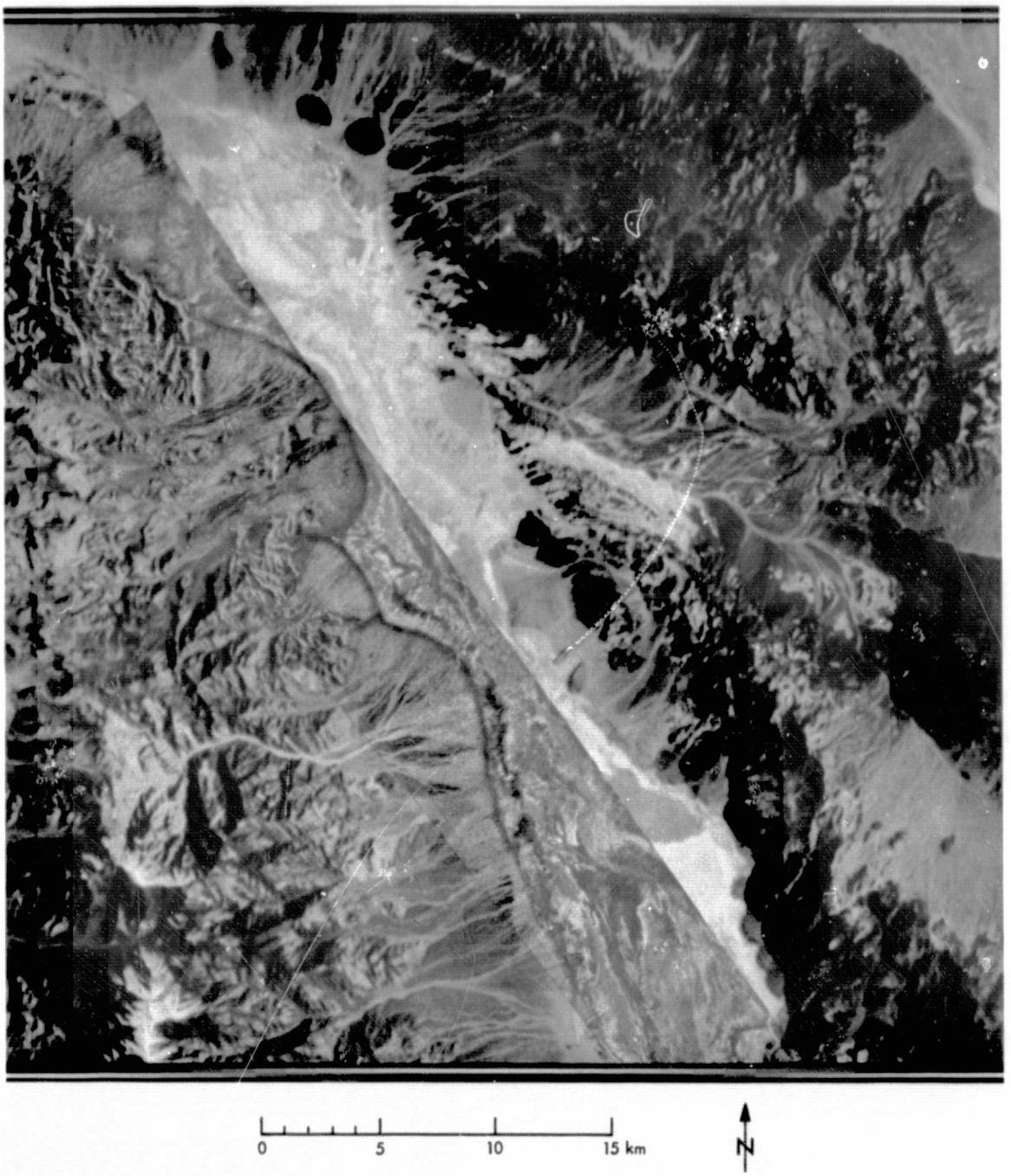

Fig. 1. Portion of LANDSAT frame 5367-17134 with two polarizations of L-band radar imagery superposed. Color code in strip: red = LANDSAT, green = LVH, blue = LVV

from near ultraviolet ($\lambda \sim 10^{-7}$ m) to microwave ($\lambda \sim 1$ m). The reflectivity of a surface depends upon:

(1) Scattering properties

  (a) Surface roughness, a measure of surface irregularity compared with sensor wavelength.

  (b) Electrical properties, including conductivity, dielectric constant, and quantum mechanical absorption/emission features.

(2) Source-target-sensor lighting geometry, including slope effects.

For visible and near-infrared wavelengths, most geological surfaces are extremely rough *isotropic* scatterers; consequently, scattering is dominated by electronic and vibrational quantum effects such as charge transfer and bending modes. Possible exceptions to this are the extremely smooth coatings on playas and desert varnishes. Advantages of such sensors are that imagery is readily interpreted and that image brightness (albedo) is dominated by relatively simple reflection-absorption properties (Goetz, et al., 1975). Disadvantages include the rather limited range of reflectivities (from 0.06 for basalts to 0.6 for the brightest salts). Utilization of information from specific absorption features has been limited by difficulties with narrow spectral filters. Another major limitation is that visible and near infrared imagery cannot be obtained through cloud cover and in the absence of solar illumination.

Thermal infrared and passive microwave image brightness is dominated by surface and subsurface *emission* properties. These are complex functions of surface roughness, surface composition, temperature, moisture, and electrical properties. Although the physical understanding of such imagery is rather difficult, lithologic discrimination by thermal inertia (using day/night image ratioing) appears promising (Kahle, et al., 1977).

Active microwave systems (imaging radars) are now being used in geologic mapping (MacDonald and Waite, 1973; Schaber, et al., 1976; Daily, 1975; and Elachi, et al., 1976). The advantages of imaging radars include control over illumination geometry, all-weather capability, and extreme sensitivity to surface roughness at scales appropriate for study of Quaternary geologic units. Radar's relative insensitivity to electrical properties in the absence of moisture is an apparent disadvantage. Such complications as penetration and resonance effects may be of actual use to lithologic mapping, as described in this report. Rather subtle differences in surface texture may have a profound effect on a surface's behavior with respect to polarization. Small variations in surface roughness exert a powerful influence on radar frequency response.

The human eye can differentiate among approximately 16 gray tones. The electro-optical scanning device used in this study resolves 256 gray tones, an increase in resolution by a factor of sixteen. The total range in reflectivity for imaging radars in desert terrains spans at least 40 dB, a factor of 2^{13}. By comparison, reflectivities in the optical region might range from 0.06 to 0.6, a factor of $2^{3.3}$. The consequence of having a ten-thousand-fold dynamic range compressed onto film is that intensity differences between two images will be indistinguishable if smaller than a factor of six. We therefore performed direct digital arithmetic, pixel-by-pixel, on pairs of imagery acquired with either differing polarization or frequency. We assumed that large deviations from a homogeneous scattering law were comparatively rare, and therefore, that the underlying reflectivity distributions were identical. For the purposes of the computer processing, then, we matched brightness histograms. As described in the image-processing section, such transformations had only small effects on the histograms, so it is unlikely that our conclusions would be affected by a more rigorous photometric decalibration.

For simplicity, we adopt the notation in Table 1 for the radar sensor configurations.

Table 1. Radar sensor configurations

Notation	Radar configuration
L(HH)	Horizontal-transmit horizontal-receive L-band (25 cm)
L(VV)	Vertical-transmit vertical-receive L-band (25 cm)
L(VH)	Vertical-transmit horizontal-receive L-band (25 cm)
X(HH)	Horizontal-transmit horizontal-receive X-band (3 cm)

In Section II we give a brief review of the geology of Death Valley. The LANDSAT imagery is discussed in Section III. Section IV includes a general discussion of the properties of radar imagery as well as a detailed analysis of the radar imagery of Death Valley. Section V contains a discussion of the synergism from combining LANDSAT and multispectral radar imagery. The digital techniques used to combine radar and LANDSAT data and to manipulate these data are presented in Section VII.

II. Geology of Death Valley

Death Valley is located in southeastern California at the south-western edge of the Basin and Range province (index

map, Fig. 2). During late Precambrian, Paleozoic and early Mesozoic times this area was the site of major geosynclines in which thick sections of limestone and clastic sediments were deposited. From late Mesozoic through early Cenozoic time, the area was subjected to folding and thrust faulting accompanied by granitic intrusions. Later in Cenozoic time the present structure of block faulted basins and ranges developed. As late as 5000 years ago, lakes occupied the floor of Death Valley. These were the product of the late Pleistocene Ice Ages. The evaporation of these lakes left thick deposits of salts and silt in the Valley. Also during this time, large alluvial fans developed (Hunt and Mabey, 1966; Nobel and Wright, 1954).

Death Valley was chosen as a test site for imaging radar studies for the following reasons: (1) low rainfall and lack of vegetation, which generally eliminates effects of soil moisture and vegetation from radar backscatter, (2) low relief of the Valley floor, which minimizes topographic distortions, and (3) wide range of roughness units which correlate well with published geologic map units (Hunt and Mabey, 1966. Schaber, et al., 1976; Matthews, 1975, pp. 399-420).

In general, the geologic units studied are Quaternary in age. These include gravel units on the surfaces of the alluvial fans; chloride, sulfate, and carbonate evaporite units and flood plain deposits on the floor of the Valley.

A. Gravel Units

Three gravel units were mapped by Hunt and Mabey (1966). The oldest, called the Number 2 gravel, forms benches up to 30 m above present washes on alluvial fans along the foot of the Panamint Mountains. These deposits also occur far upstream from the gravel fans. The Number 2 gravel is overlapped by younger gravels and is more bouldery and better cemented. Drainage on the Number 2 gravel preserves the original fan form even though there has been much faulting and tilting. The surface of the Number 2 gravel is smooth desert pavement created from the disintegration of originally round, stream worn pebbles, cobbles, and boulders. On most Number 2 gravel surfaces 75% or more of the boulders and cobbles have lost their original roundness. Pavements composed of disintegrated pebbles and cobbles are the smoothest in the Valley. These rocks form a smooth interlocking surface usually one layer thick. The layer is underlain by silt of variable thickness – usually only a few centimeters. This kind of surface has a high runoff and low permeability. Runoff usually occurs as sheet wash.

The Number 3 gravel is less well cemented than the No. 2 gravel. The range in grain size is smaller, from pebble to cobble size with few boulders. The Number 3 gravel is neither as thick nor as extensive as the Number 2 gravel and often forms only a thin veneer over the latter. The surface of the Number 3 gravel is generally less than 10 feet above the recent washes. The Number 3 gravel is displaced by few faults. The gravels are less weathered and have a darker coating of desert varnish than the Number 2 gravel.

Desert varnish is a dark brown to black coating that forms on exposed surfaces of rocks of all lithologies in most desert regions. Recent work by Potter and Rossman (1977a) indicate that the coating is composed of 70-90% clay minerals with a small amount of manganese and iron oxides that supply the color. Materials for the varnish appear to be derived from other than the rock substrate, and Potter and Rossman (1977b) suggest that they are derived from windblown sediment.

Gravel Number 4 occupies the recent washes on the gravel fans. On the high parts of the fans the washes are incised lower than the older gravels, but on the lower parts the Number 4 gravel overlaps the Number 3 gravel. The Number 3 gravel overlaps the Number 2 gravel higher up (Fig. 3).

The Number 4 gravel does not extend significantly onto the saltpan. The abrupt lower limit coincides with a break in slope at the foot of the fans. The lower edges of the fans slope 2 to 6%, while the edge of the saltpan slopes less than 1%. The deposits are a maximum of about 3- to 5-m thick. They are composed of firm rocks without much weathering or desert varnish. Most of the Number 4 gravel is derived from older gravels. It is composed of loose gravel with few boulders and little sand. Additional studies of alluvial fans in desert regions can be found in Denny (1965) and Hooke (1967).

B. Saline Units

The Death Valley saltpan formed in and around a lake that occupied the Valley about 2000 years ago. The pan covers about 500 square km, all of which is below sea level. The salt crust ranges from a few centimeters to a few meters thick and is underlain by silt and clay. The center and lowest part of the pan is composed of chloride salts. This is surrounded by a zone of sulfate salts which is, in turn, surrounded by a sandy zone containing carbonate salts. This zoning is a reflection of the different solubilities of the salts. The deposits are a few centimeters to a few meters higher than the areas subject to flooding at present.

The massive rock salt unit (Qh) covers about 20 km^2 of the lowest part of the salt pan at an elevation of -85 m. It has an exceedingly rough surface of jagged pinnacles 15-25 cm wide and 30-70 cm high, that has earned the name "Devil's Golf Course." The deposit is about 95% sodium chloride, suggesting that it is the residue of the last lake to flood Death Valley.

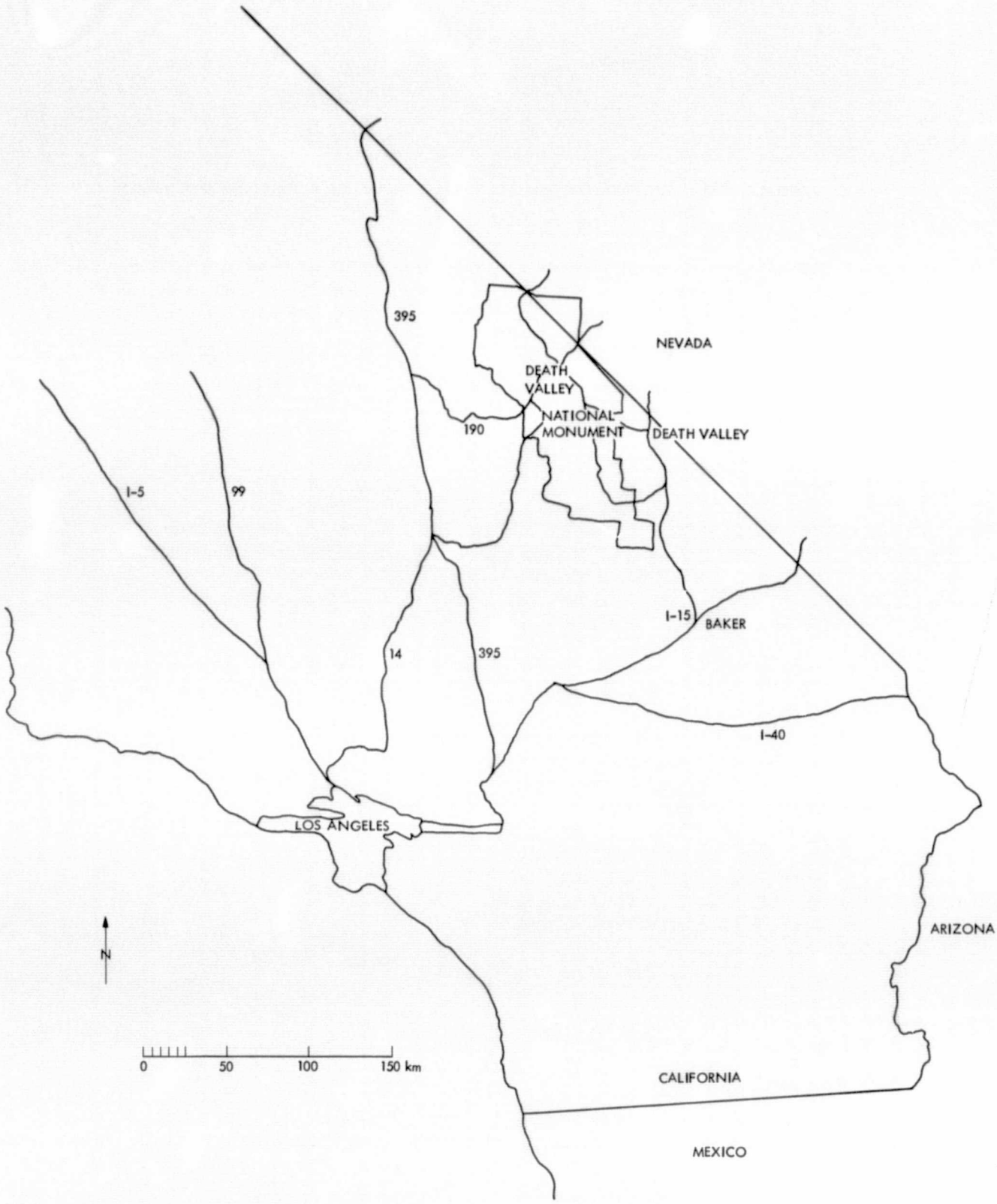

Fig. 2. Index map showing location of Death Valley

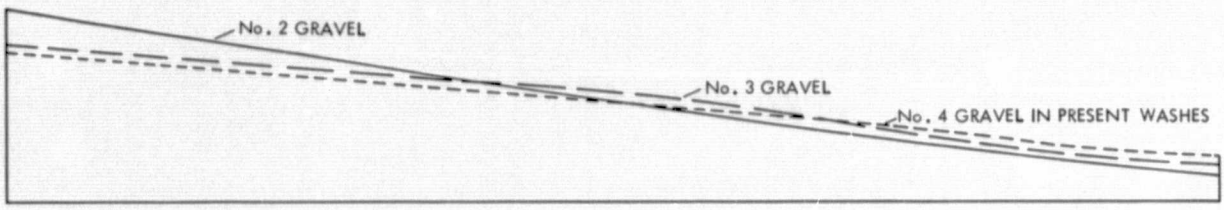

Fig. 3. General profile of fans along the west side of Death Valley, illustrating overlap of younger gravel on older gravels

The rough silt rock salt unit (Qhr) is in gradational contact with Qh and covers about 50 km^2. It is equally rough but contains 20 to 40% silt. It is elevated about 2-4 m above Qh (-83 to -81 m). The composition and distribution of this unit indicates that it formed in the shallow margins and mud flats of a lake that suffered seasonal fluctuations in depth.

The rough silty rock salt (Qhr) is in gradational contact with the smooth silty rock salt unit (Qhs) that forms large, smooth plains at the mouths of the principal streams of Death Valley. The elevation of the deposits is about 79 m below sea level, and the area is about 130 km^2. They consist of a layer of brown silt 2-15 cm thick underlain by about 30 cm of silty rock salt. The deposits were probably formed from the evaporation of ground water that was later smoothed and covered with silts by floods from the adjacent streams.

The chloride zone is surrounded by a discontinuous belt of massive gypsum (Qsg) at -81 m to -82 m elevation. The gypsum overlies damp or wet silt and is capped by 2-15 cm of anhydrite or bassanite. All the present-day gypsum deposits are located near marshes (Qsm), suggesting that the massive gypsum formed in marshes at a time of higher ground water discharge from nearby springs.

The last unit important to radar studies of Death Valley is the flood plain unit (Qf). These deposits are lowest in elevation and subject to seasonal flooding. They comprise about a third of the saltpan. The seasonal flooding of these areas produces a very smooth playa surface with a very thin salt crust. Some areas peripheral to the flood plain deposits are infrequently flooded. The evaporation of this ground water leaves a rougher crust of silty rock salt.

III. LANDSAT Imagery

LANDSAT 1 and 2 (formerly ERTS 1 and 2) orbit the Earth at an altitude of approximately 900 km in steeply inclined orbits that allow them to image nearly the entire surface of the Earth. Each satellite passes over the same spot on the Earth every 18 days at about 9:00 a.m. local time. A multi-spectral scanner (MSS) on each LANDSAT provides imagery in four spectral bands. Bands 4, 5, 6 and 7 span the wavelength ranges 0.5-0.6 μm (green), 0.6-0.7 μm (red), 0.7-0.8 μm (IR1), and 0.8-1.1 μm (IR2), respectively. Each image is obtained by 24 detectors, six to each band. A mirror scans perpendicular to the flight path, producing a swath width of 11.5 deg, or 185 km on the ground. This wide swath provides a synoptic view useful for large-scale studies. The resolution of the MSS imagery is about 80 m (Fig. 4).

The signals generated by the MSS detectors are a function of: (1) surface spectral reflectance, (2) solar irradiance at the surface, (3) atmospheric transmission, (4) instrument responses, and (5) scattering of sunlight by the atmosphere along the detector line of sight. Generally, in a good cloud-free LANDSAT frame all parameters but the first are nearly constant.

Reflectance of rocks and minerals in the visible and near infrared regions of the spectrum are controlled by electronic

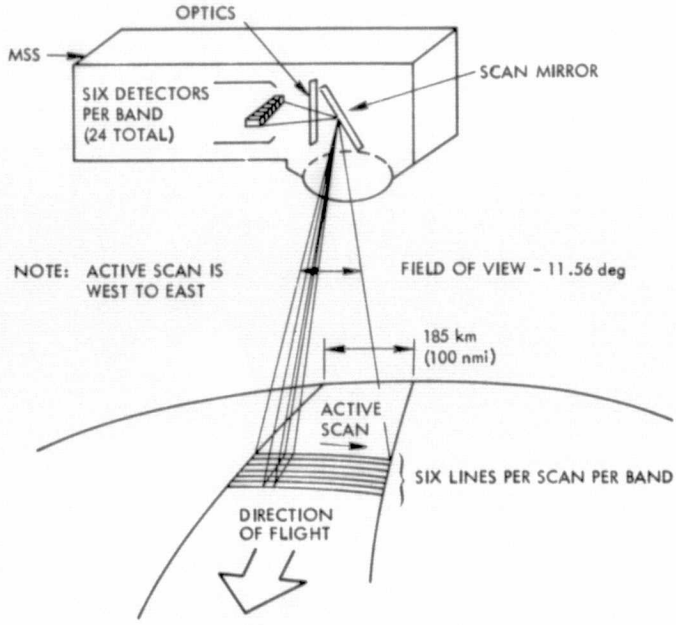

Fig. 4. Multispectral scanner (MSS) geometry

transitions in transition metal ions and, in the shorter wavelengths, by electron charge transfer between ions. Iron in its two oxidation states is responsible for the color of most rocks in the field. Interactions of the iron ions with their surrounding crystal fields produce some color phenomena (Burns, 1970; Karr, 1975; Hunt and Salisbury, 1970 – 1976).

Because the MSS sees only the weathered surfaces of rocks, the use of spectral reflectance to determine rock type is difficult. The spectral reflectivity of weathered rocks is controlled by the abundance and oxidation state of iron. Another problem arises when there is significant vegetation cover. Vegetation has a high reflectance in the near infrared that makes bands 6 and 7 of little use for the spectral discrimination of rock types in heavily vegetated areas (Goetz, et al., 1975; Rowan, et al., 1974).

The LANDSAT frame used in this study was obtained on April 20, 1976. Figure 5 shows a standard color composite obtained from EROS Data Center. In this image, band 4 is coded blue, band 5 is coded green, and band 7 is coded red. Because of the lack of vegetation and other significant differences in spectral reflectivity, very little color is seen in the false color composite. Furnace Creek Ranch appears bright red because of irrigated vegetation at the resort.

In examining the frame several features are easily discernible. Differences in albedo are apparent in the mountains, on the giant gravel fans on the west side of the valley, and on the salt pan at the bottom of the valley. Several linear features are also visible.

Several areas in the mountains around Death Valley show differences in the four bands, which correlate well with geology as mapped by Hunt and Mabey (1966). Light and dark areas in the northern Black Mountains shown on the LANDSAT false color composite image correlate with Miocene or Pliocene playa deposits of the Furnace Creek formation and Tertiary volcanics plus fanglomerate of the Funeral Formation, respectively. Three dark spots north of Cottonball Basin are shown as Miocene (?) sedimentary rocks. Some layering is apparent in the mountains 10 km west of Cottonball Basin which correlates with late Paleozoic carbonates and quartzites steeply dipping to the east. The simplified geologic map (Fig. 6a) lumps the above units together.

Albedo variations on the alluvial fans in Death Valley reflect differences in amount of desert varnish. The most recent washes (Qg_4) show up light in color. They are frequently abraded and, therefore, have less desert varnish than older areas of desert pavement. The fact that the older desert pavement areas have a different surface roughness makes little difference to the MSS. The older gravels on the fans (Qg_2 and Qg_3), therefore, have very similar spectral signatures.

It is difficult to distinguish many of the evaporite units on the Death Valley Salt Pan by spectral reflectivity alone. Both the smooth and rough silty rock salt units (Qhs and Qhr) 10 km south of Furnace Creek Ranch and massive rock salt unit (Qh) in Badwater Basin have similar grey tones due to included silt within the salt or shadowing effects in the rougher units, as discussed in Section V. Very light tones characterize flood plain deposits (Qf) with their thin salt crusts, the "cleaner" saline units such as eroded salt (Qhe), and the carbonate zone of the saline facies (Qch). The smooth silty rock salt unit (Qhs) in Cotton Ball Basin also appears light colored.

Two prominent linear features are apparent trending northwest-southeast about 5 and 12 km northeast of Cottonball Basin. These features consist mainly of abrupt changes in slope, topography, or albedo and are shown on Hunt and Mabey's (1966) geologic map as high angle normal faults. The fault furthest from Cottonball Basin is named the Keane Wonder Fault. A discontinuity in albedo is visible on the lower Hanaupah Canyon fan about 1 km west of its end. This is shown on the map as a steep, normal fault called the Hanaupah Escarpment. The change in albedo is caused by an abrupt change from Qg_2 with its dark stain of desert varnish on the west to younger Qg_3 and Qg_4 gravels with less varnish on the east.

The LANDSAT frame of Death Valley shows several features of geological interest, including details of desert varnish distribution on the alluvial fans, some details in the saltpan, and linear features related to faulting.

Similar tonal variations in conventional photography have been described in the Sahara Desert by Smith (1969). He found consistent tonal values as shown in Table 2.

Table 2. Tonal value

	Sahara	Death Valley (this work)
Lightest	Thin salt crusts	Qf
	Quartzose sand (channel and dune)	Qg_4
	Dry compact clayey surfaces	Qf
	Rough massive salt (sometimes silty)	Qh
	Iron-stained dune sand	
	Moist clays	Qf
	Rough gravels	Qg_3
Darkest	Desert pavements	Qg_2

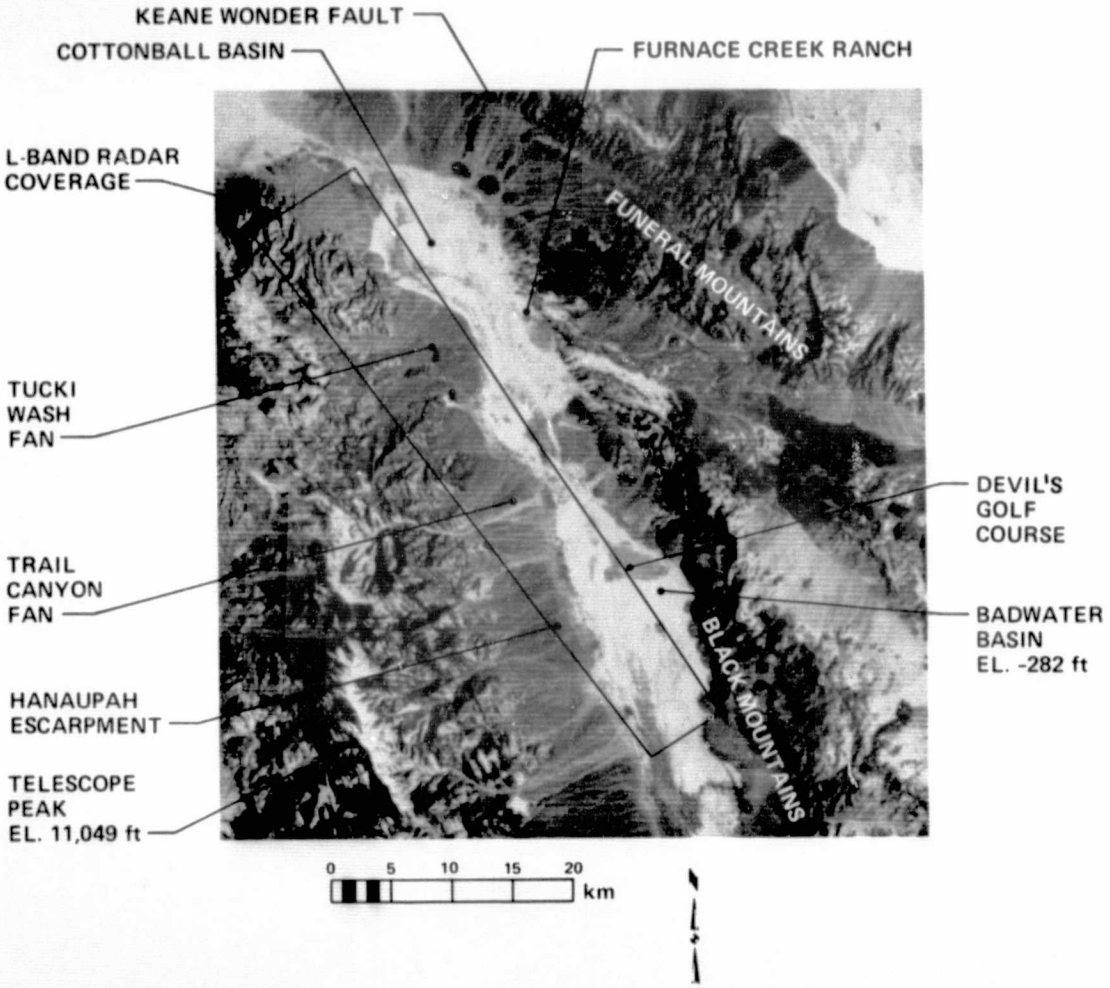

Fig. 5. Eros standard color composite of a section of LANDSAT frame 5367-17134 obtained April 20, 1976. Red = Band 7, Green = Band 5, Blue = Band 4

FOLDOUT FRAME

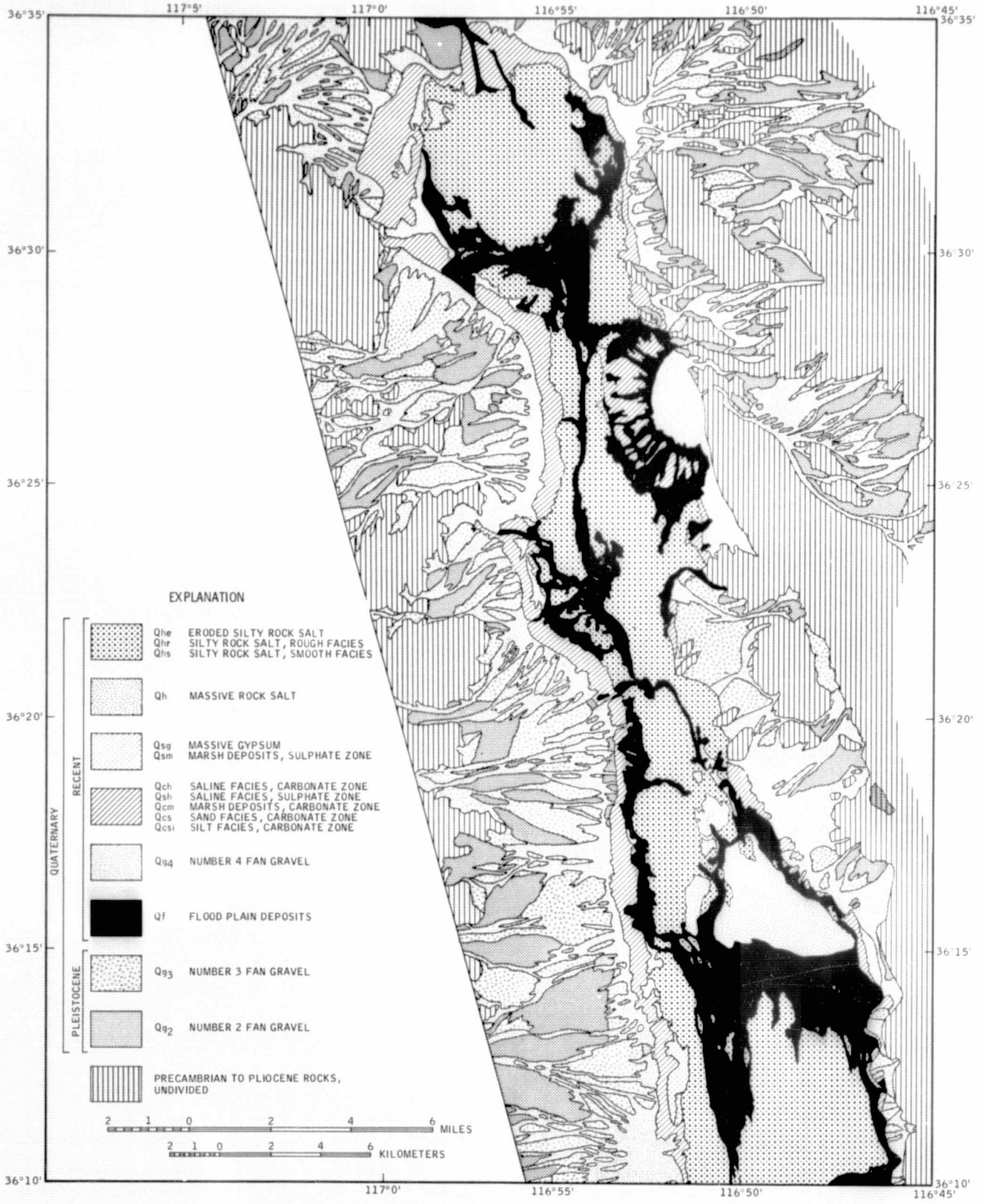

Fig. 6a. General geologic map of Death Valley modified from Hunt and Mabey (1966)

FOLDOUT FRAME 2

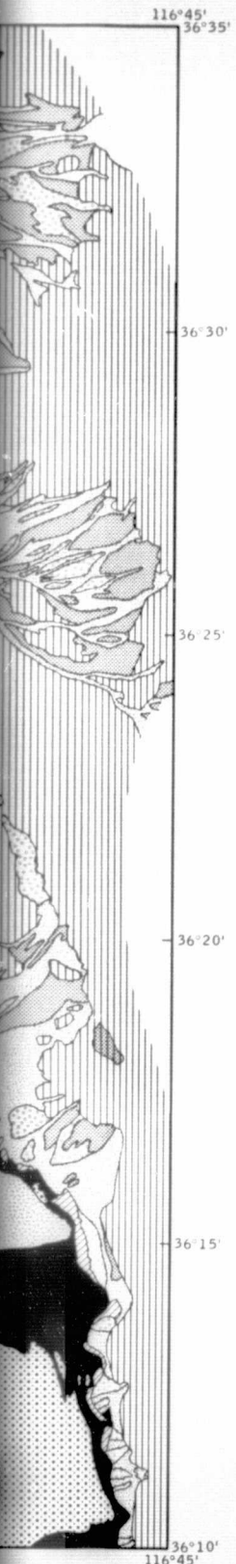

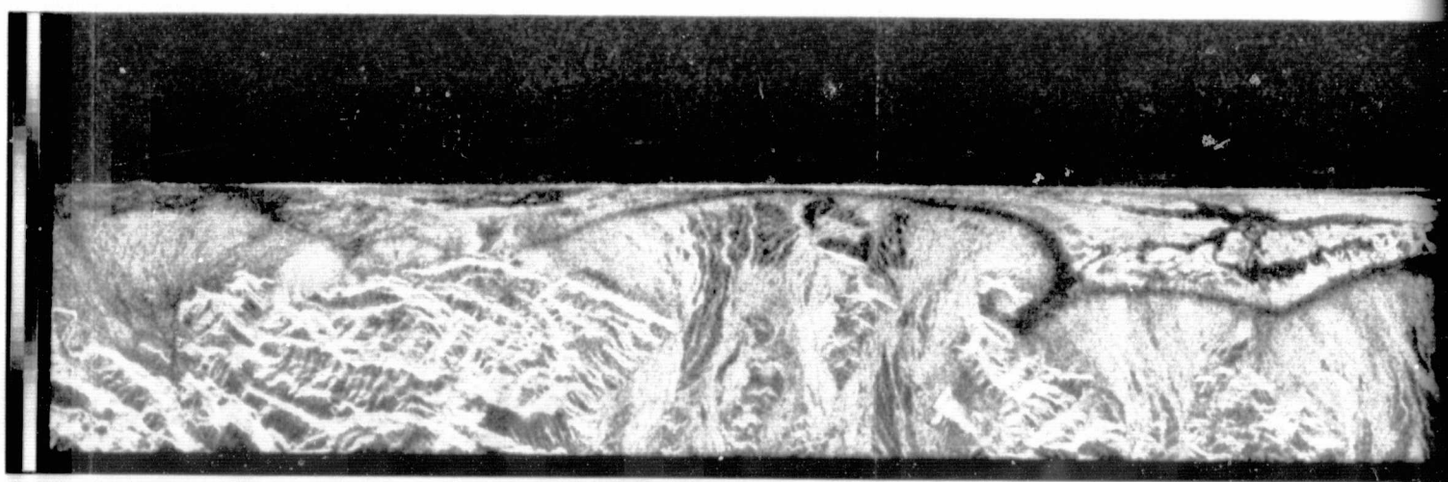

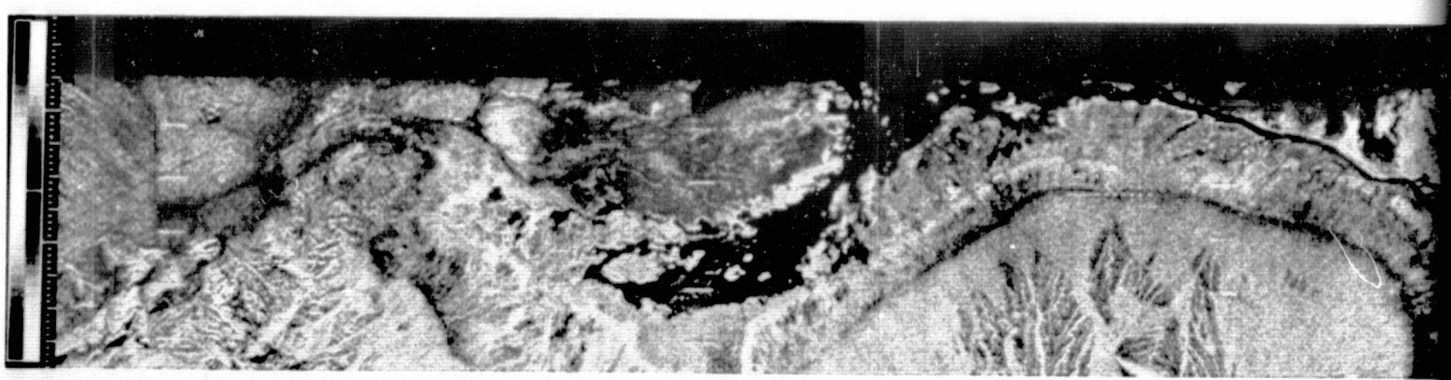

66)

FOLDOUT FRAME 3

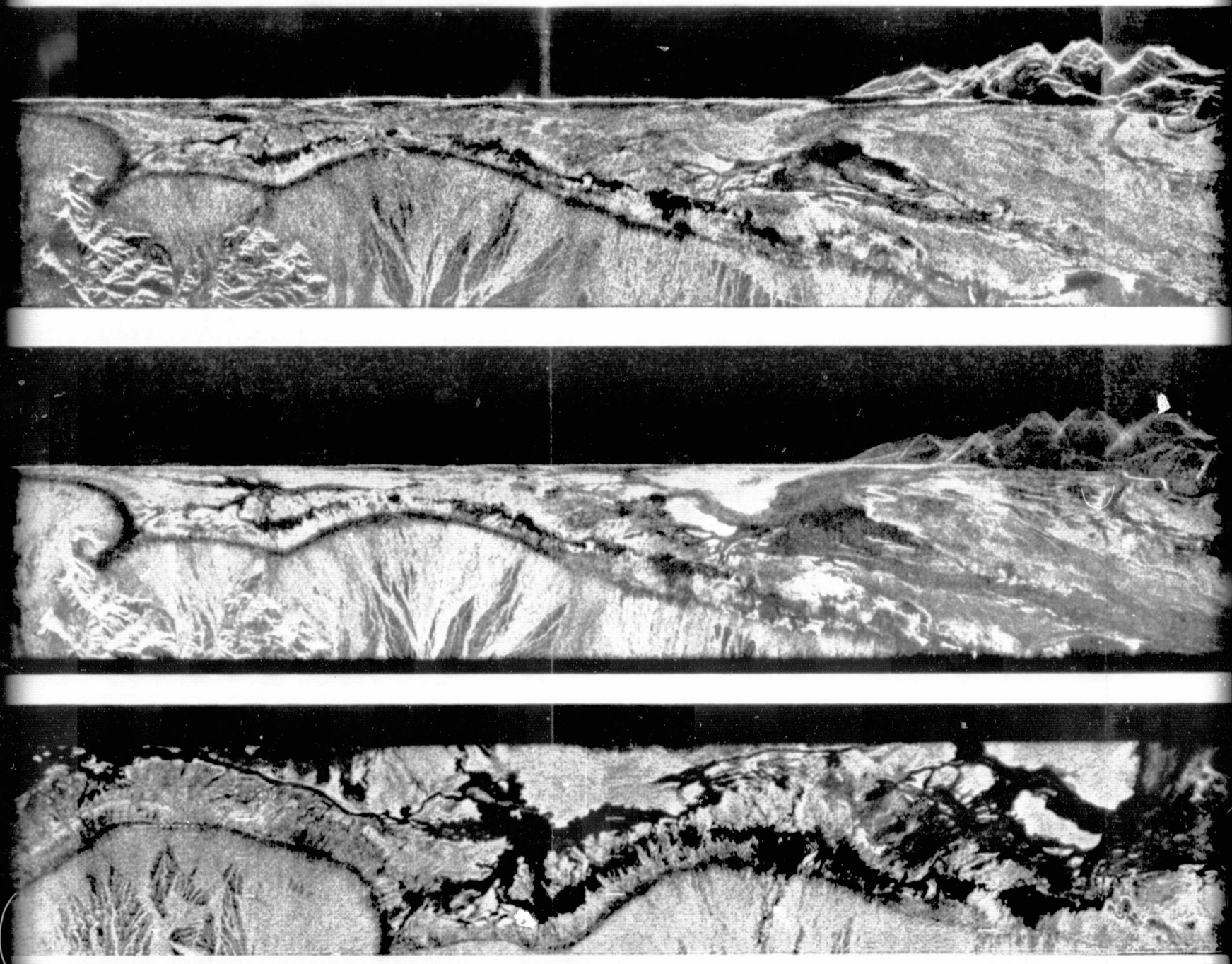

Fig. 6b. Radar imagery of Death Valley

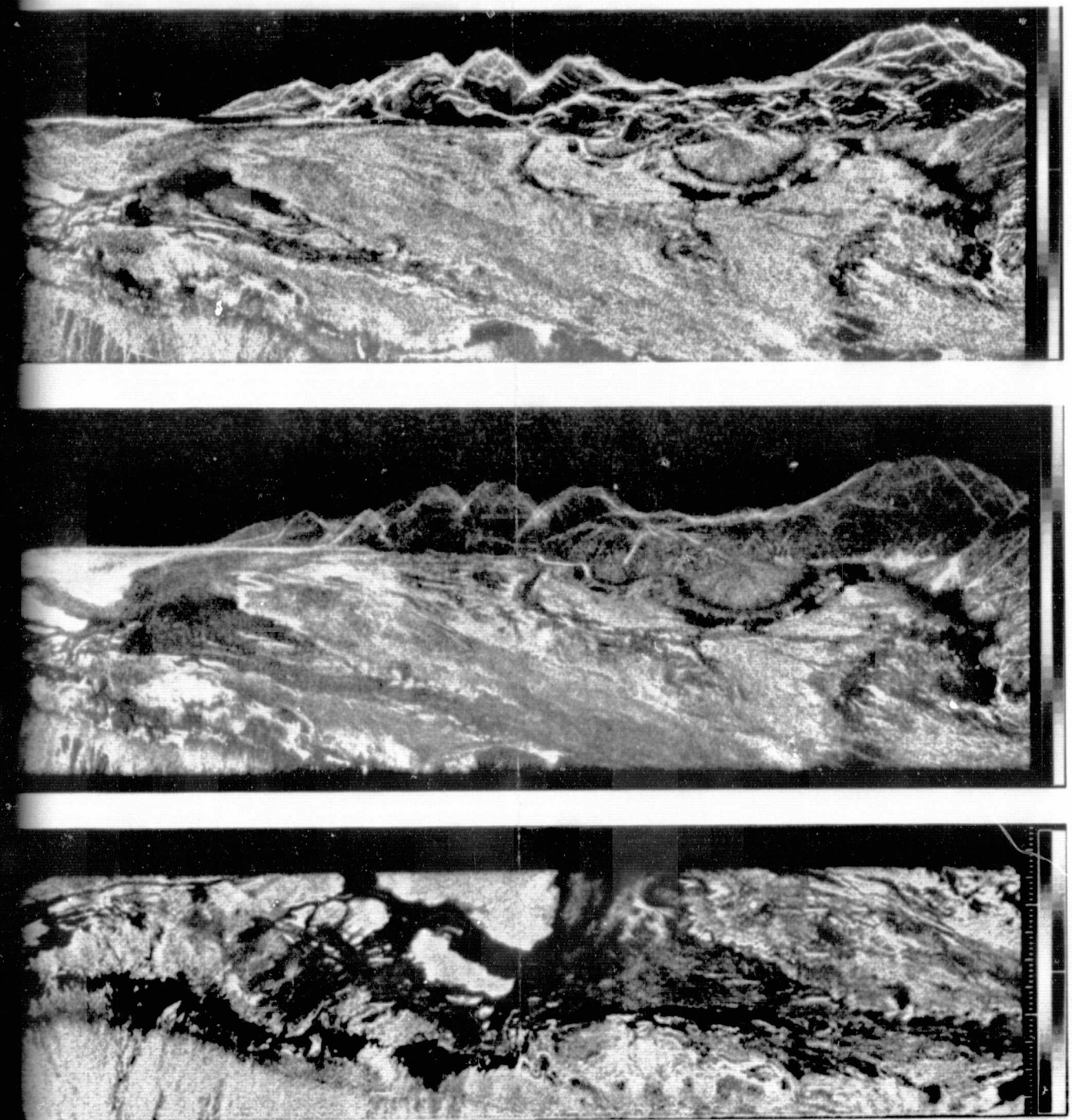

Fig. 6b. Radar imagery of Death Valley: LVV (top); LVH (center); and XHH (bottom)

IV. Radar Imagery

Airborne imaging radars are being employed quite extensively by exploration companies and user agencies for geologic mapping and large-scale surveys for sites of potential mineral deposits. There are two classes of information that can be extracted from radar images. First, they are used in a similar way to visual photography to extract morphological information. They clearly show topographic features, lineaments, fault scarps, drainage patterns, vegetation lines and geologic units of varying roughness or moisture content. The geometric presentation of radar imagery is somewhat different from that of conventional photography; however, most of the available photo interpretation techniques can be used to interpret radar imagery.

The second class of information is more unique to radar, and it consists of using the image brightness in each resolution cell to characterize the surface properties. The image brightness is directly related to the radar backscatter; which, in turn, is a function of parameters related to the surface roughness, average slope and dielectric constant. The use of this class of information requires a good quantitative understanding of the radar scattering from geologic surfaces, especially the behavior of the surface signature as a function of the imaging radar frequency, polarization and observation geometry (i.e., look-angle and direction). Research relating detailed surface roughness statistics in Death Valley to radar return is being completed by Schaber, et al. (in preparation). Of particular interest is the synergism of using multiple imaging parameters, such as simultaneous imagery, at different radar frequencies and polarization, and extending this synergism to the use of simultaneous radar/IR/visible imagery.

In this section we review and briefly discuss the present understanding of radar scattering from geologic surfaces. The emphasis will be on the physical interpretative meaning of the backscatter, rather than the detailed mathematical derivation. Therefore, with little discussion, we will start with the theoretical results reported by other authors in the open literature. However, we will discuss in some detail how these results can be best used to interpret radar imagery of geologic surfaces. Some of these results are used in the geologic analysis reported in this paper. The rest will be the subject of future research.

The reader must keep in mind that geologic surfaces cannot be described in a simple mathematical form, which means that it is difficult to derive exactly the scattering properties of a specific surface. The best we expect is to derive quasi-quantitative criteria and techniques that would allow the extraction from radar images of some reasonably specific information about the surface.

A. Radar Scattering From Geologic Surfaces

The theoretical treatment of the scattering of electromagnetic waves from rough surfaces and bodies of given shapes has been the subject of many papers and books over the last thirty years (Beckmann and Spizzichino, 1963; Valenzuela, 1967). In the case of rough surfaces, a number of theories have been developed that would allow a reasonably good understanding of the behavior of the backscatter cross-section as functions of the surface properties and the sensor parameters. These theories are based on the use of perturbation techniques and Bragg-Rice theory for slightly rough surfaces (irregularities that are small relative to the wavelength), and physical optics techniques for surfaces with a relatively large radius of curvature. Exact scattering solutions have also been developed for general rough surfaces. However, they require extensive numerical calculations, and they are not amenable to simple interpretation.

In the case of bodies of given shape (i.e., spheres, ellipsoids, cylinders, edges) a number of approximate solutions, as well as exact (analytical or numerical) solutions, have been derived (Ruck, et al., 1970). It should be pointed out that in most of the papers published, the main emphasis is on the behavior of the amplitude of the scattered wave. Only recently have scientists started to study the problems of depolarization of the scattered echo and evaluate the information content in the depolarized signal.

The topography and roughness of geologic surfaces, in general, cannot be described in an exact mathematical form, which makes it hard to decide which theory must be used. The best that can be expected for is to categorize a surface in a relatively broad category for which the closest theoretical model can be used. To illustrate, in Fig. 7 we show four different kinds of surfaces encountered in Death Valley. The first area (Fig. 7a) can be described as a slightly rough surface (for L-band signals), and thus the Bragg-Rice theory would be the most applicable. Figure 7b represents a rougher region, and in this case the Bragg-Rice theory can only be marginally applicable. Figure 7c illustrates an area which can be considered consisting of a finite number of bodies with an ellipsoidal shape. Figure 7d corresponds to an area with a large number of finite bodies whose overall effect might be represented by a rough surface.

B. Scattering Properties of Rough Surfaces

The backscatter cross sections of a slightly rough surface has been derived by Valenzuela (1967, 1968) and others using the Rice-Bragg theory. He derived the expressions for the direct polarization cases (HH for horizontal polarization during transmission and reception, VV for vertical polarization during transmission and reception) and cross-polarized case

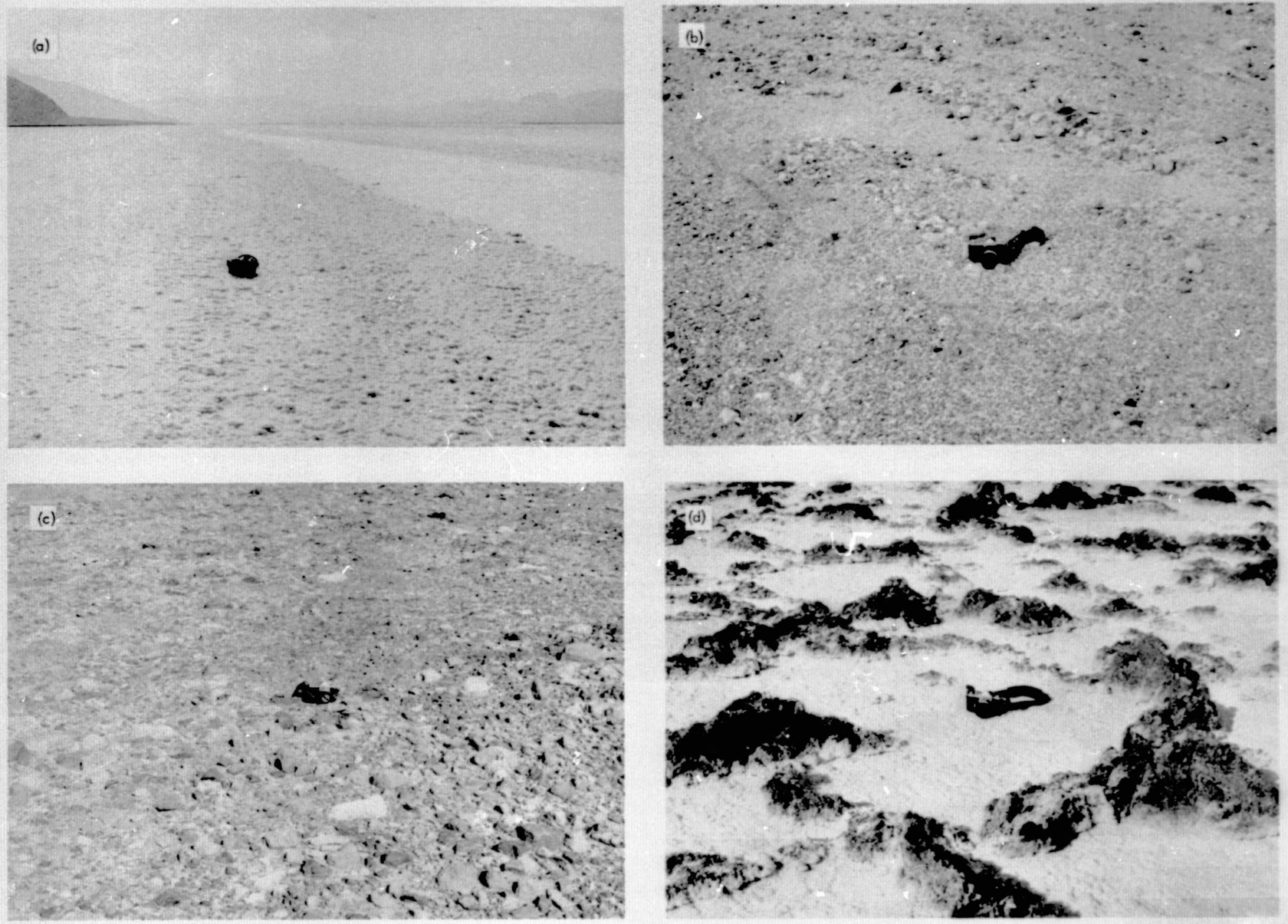

Fig. 7. Example of different scattering surfaces: (a) slightly rough surface (Qf), (b) rougher Bragg surface (Qg_2), (c) finite number of bodies (Qg_3), and (d) large number of bodies approximating rough surface (Qh)

(HV for horizontal polarization during transmission and vertical polarization during reception. The VH case is identical to the HV case). The results are (see geometry in Fig. 8):

$$\sigma_{HH} = AW(K_x, K_y) + CI$$

$$\sigma_{VV} = BW(K_x, K_y) + CI$$

$$\sigma_{HV} = DW(K_x, K_y) + EI$$

$$A = 4\pi\beta^4 \cot^4 \theta_i \left[\alpha^2 \cos^2 \delta T_1 + \sin^2 \delta T_2\right]^2$$

$$B = 4\pi\beta^4 \cot^4 \theta_i \left[\alpha^2 \cos^2 \delta T_2 + \sin^2 \delta T_1\right]^2$$

$$C = 2\pi\beta^8 \cot^4 \theta_i \sin^2 \theta \sin^2 2\delta T_3^2$$

$$D = \pi\beta^4 \cot^4 \theta_i \alpha^2 \sin^2 2\delta \left[T_2 - T_1\right]^2$$

$$E = 2\pi\beta^8 \cot^4 \theta_i (\alpha^2 \cos^2 \delta - \sin^2 \delta)^2 T_3^2$$

$$T_1 = (\epsilon - 1) \Big/ \left[\cos \theta \cos \delta + \sqrt{\epsilon - \sin^2 \theta_i}\right]^2$$

$$T_2 = (\epsilon - 1) \left[(\epsilon - 1) \sin^2 \theta_i + \epsilon\right] \Big/ \left[\epsilon \cos \theta \cos \delta + \sqrt{\epsilon - \sin^2 \theta_i}\right]^2$$

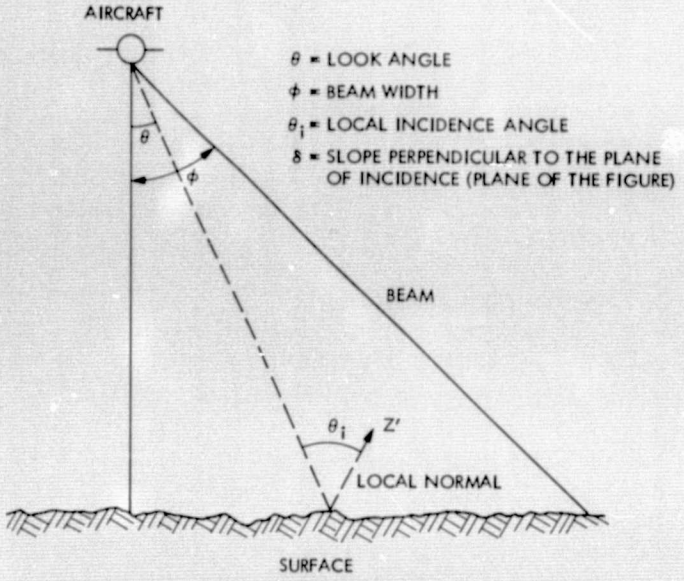

Fig. 8. Imaging radar geometry

$$T_3 = (\epsilon - 1)^2 \sqrt{\epsilon - \sin^2 \theta_i} \Big/ \left(\cos \theta \cos \delta + \sqrt{\epsilon - \sin^2 \theta_i}\right) \left(\epsilon \cos \theta \cos \delta + \sqrt{\epsilon - \sin^2 \theta_i}\right)^2$$

$$I = \int_{-\infty}^{\infty} dp \int_{-\infty}^{\infty} dg\, p^2 g^2 \frac{W(p - \beta \sin\theta, g)\, W(p + \beta \sin\theta, g)}{\left|d(p,g) D_{pg}\right|^2}$$

$$d(p,g) = \sqrt{\beta^2 - (p^2 + g^2) \sin^2 \theta} + \sqrt{\epsilon\beta^2 - (p^2 + g^2) \sin^2 \theta}$$

$$D_{pg} = \sqrt{\beta^2 - (p^2 + g^2) \sin^2 \theta} \sqrt{\epsilon\beta^2 - (p^2 + g^2) \sin^2 \theta} + (p^2 + g^2) \sin^2 \theta$$

where

δ = tilt angle perpendicular to the plane of incidence

θ = look angle

θ_i = actual incidence angle

α = $\sin \theta$

γ = $\cos \theta$

α_i = $\sin \theta_i$

γ_i = $\cos \theta_i = \cos \theta \cos \delta$

β = $2\pi/\lambda$

λ = radar wavelength

$W(p,g)$ = energy spectral density of the surface

The above expressions appear to be complicated, but they can be easily interpreted; and, with some simplification, they can be used to understand the behavior of the different backscatter cross-sections as a function of sensor parameters and surface characteristics.

1. Effect of the Surface Roughness

The term $W(K_x, K_y)$ basically corresponds to single Bragg scattering from the spectral component of the surface roughness which satisfies the Bragg condition for the frequency and look-angle of the radar sensor. Physically, the Bragg condition corresponds to the case in which the projected radar wave vector is equal to half the wave vector of a certain spectral component of the surface (Fig. 9). This would lead to a resonance effect (i.e., conservation of momentum or wave vector) which results in a strong return. For a given radar frequency and look-angle, only one spectral component of the surface satisfies the Bragg condition. Thus, the imaging radar acts like a spatial filter and the brightness in the image is directly proportional to the amplitude of the roughness spectral component which satisfies the Bragg condition.

To illustrate, for a look-angle of θ, the imaging radar will be most sensitive to the surface roughness wavelength Λ which is equal to $\Lambda = \lambda/2 \sin \theta$, where λ is the radar wavelength (i.e., for $\theta = 45$ deg, $\Lambda = \lambda/\sqrt{2}$ which gives $\Lambda = 18$ cm for $\lambda = 25$ cm and $\Lambda = 2.1$ cm for $\lambda = 3$ cm).

The terms A, B, C, D, and E are mostly related to the Fresnel reflection of the surface, which is independent of the roughness, and is dependent on the geometry and surface dielectric constant.

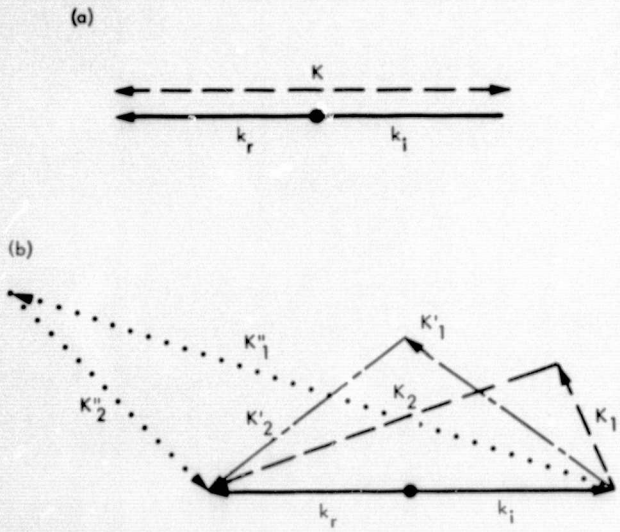

Fig. 9. Conservation of wave vector: (a) Single Bragg scattering. The incident wave vector k_i can be transformed into the returned wave vector k_r by the mean of only one surface roughness wave vector K; (b) double Bragg scattering. An infinite number of combinations of pairs of surface wave vectors can transform k_i into k_r. This implies that the strength of the returned wave is related to the overall roughness spectrum with a well-defined weighting function

The term I corresponds to a double Bragg resonance effect, i.e., the electromagnetic wave resonates with two spectral components of the surface roughness. As illustrated in Fig. 9, there is an infinite number of combinations that would allow resonance, hence the integral in the expression for I. This implies that I is related to the overall roughness spectrum, whereas W is related to only one component of that spectrum.

In the case of small δ, the expressions for the backscatter cross-sections can be simplified. To the first order of approximation σ_{HH} and σ_{VV} are proportional to W, i.e., to a specific spectral component of the surface roughness which satisfies the Bragg condition. Meanwhile σ_{HV} is proportional to I, i.e., to an integral over the roughness spectrum with a certain kind. This leads to our first hypothesis:

> "The brightness in the direct polarization imagery is mostly sensitive to the surface roughness at the spectral component which satisfies the Bragg condition. The brightness in the cross-polarized imagery is more sensitive to the overall roughness spectrum than the like polarization."

Another interesting point is that, for small δ, the ratio σ_{HH}/σ_{VV} is independent of W, i.e.,

$$\sigma_{HH}/\sigma_{VV} = A/B$$

and is dependent only on the observation geometry, surface average slope and surface dielectric properties. Figure 10 shows behavior of σ_{HH}/σ_{VV} for different cases. This leads to the second hypothesis:

> "The image that results from taking the ratio of two images taken in the direct polarization mode (i.e., HH or VV) is little sensitive to the surface roughness. The simultaneous analysis of the (HH/VV) image and of the HH, VV, or HV images should help in the separation of the roughness effects from the topographic and dielectric effects."

2. Effect of Surface Slope

Let us first consider the tilt angle perpendicular to the plane of incidence, i.e., δ. For small values of δ, A, and B (i.e., σ_{HH} and σ_{VV}) are proportional to $\cos^2 \delta$, while E (i.e., σ_{HV}) is proportional to $\cos^4 \delta$. This implies that σ_{HV} is more sensitive to δ than either σ_{HH} or σ_{VV}. This hypothesis has been confirmed numerically for large ϵ by Valenzuela (1968) even for relatively large values of δ. The results of Valenzuela showed that σ_{VV} is practically insensitive to δ, σ_{HH} is sensitive to δ only at large ($\gtrsim 65$ deg) incidence angles, while σ_{HV}

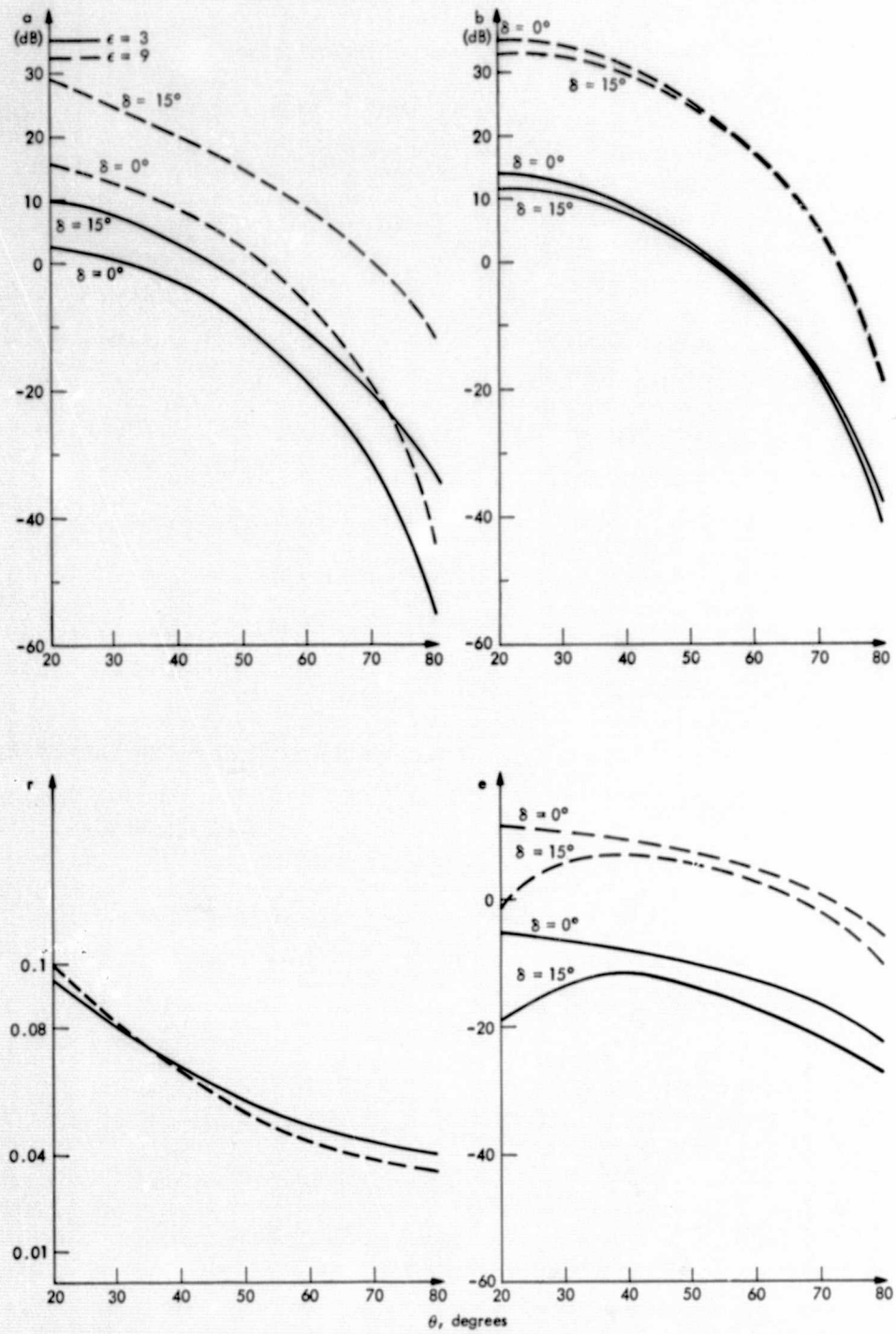

Fig. 10. Behavior of the coefficients in the direct and cross-polarized cross sections. $a = \log (A/4\pi\beta^4)$ illustrates the general behavior of σ_{HH}. $b = \log (B/4\pi r\beta^4)$ illustrates the general behavior of the coefficients σ_{VV}. $r = a/b = A/B$ illustrates the behavior of σ_{HH}/σ_{VV}. $e = \log (E/2\pi\beta^8)$ illustrates the general behavior of the coefficient in σ_{HV}. These curves do not include the contribution of the roughness spectrum

is sensitive to δ at practically all angles. This was also confirmed for small ϵ as shown in Fig. 10 where we plotted the behavior of A, B, and E. This leads to our third hypothesis:

> "For incidence angles between 20 and 65 deg the brightness in the direct polarization imagery is little sensitive to the slope angle δ in the direction perpendicular to the plane of incidence, while the cross-polarized imagery is sensitive to this slope. For larger incidence angles only the vertical polarized imagery is little sensitive to δ."

Let us now consider the effect of θ, which is the look-angle (a change in θ is similar to a change of the surface slope in the plane of incidence). From Fig. 10 we see that usually σ_{VV} is larger than σ_{HH}. Both are also larger than σ_{HV} for a slightly rough surface. However, this is not true in very rough surfaces where the cross polarized might be larger than the direct polarized return.

Figure 10 also shows that the vertical polarized image should be somewhat less sensitive to θ than the horizontal polarized image. The comparison of the behavior, as a function of θ, of the direct and the cross-polarized images cannot be generalized, because they depend strongly on W and I. However, Valenzuela (1966) studied the case of large θ and an isotropic spectral density that has an inverse fourth order behavior as a function of the wave vector. From his curves, it can be seen that there is similar dependence of σ_{HV} and σ_{VV} as a function of θ. In other terms, σ_{HV}/σ_{VV} is not very sensitive to θ. This leads to a fourth hypothesis:

> "It seems that in some cases the ratio image of the vertical direct (VV) and cross-polarized images should have little sensitivity to the slope in the plane of incidence."

3. Effect of Surface Dielectric Constant

The backscatter in all different polarization configurations increases with ϵ. This results from the simple fact that the Fresnel reflectivity is higher for larger dielectric constant discontinuity at the reflecting interface. In the case of large ϵ and $\delta = 0$ it can be shown that σ_{HH} is little dependent on ϵ, σ_{VV} is proportional to $\epsilon^{1/2}$ and σ_{HV} is proportional to ϵ. This behavior can also be seen in Fig. 10 for σ_{HH} and σ_{VV}. This leads to the fifth hypothesis:

> "In general the horizontally polarized imagery is the least sensitive to the dielectric constant, while the vertically polarized and the cross-polarized imagery are the most sensitive to the dielectric changes."

4. Summary for Rough Surfaces

Based on some simplification of the theoretical expression of backscatter from rough surfaces, a number of hypotheses can be drawn that can help in the interpretation of radar imagery. These hypotheses have still to be tested through actual radar data and field mapping.

These hypotheses are summarized as follows:

(1) Cross-polarized imagery is a better indicator of the average surface roughness. Direct-polarized imagery gives information on the roughness at a specific scale that is approximately equal to that of the observing wavelength.

(2) The ratio of VV and HH images is little sensitive to surface roughness.

(3) The ratio of VV and HV images is little sensitive to slope in the plane of incidence.

(4) VV imagery is little sensitive to slope in the direction perpendicular to the plane of incidence. HV imagery is the most sensitive to slope in this direction.

(5) The HH imagery is the least sensitive, while HV and VV imagery are the most sensitive to the surface dielectric constant changes.

C. Scattering From Finite-Shaped Bodies

A number of techniques have been used to study the backscatter from finite shaped bodies. In the case of simple shapes (i.e., spheres, cylinders, cones, wedges) exact theoretical solutions were derived. However, in the case of general shapes, numerical or approximate techniques have to be used. The simplest approximation is for the case where the radar wavelength is large relative to the dimensions of the scattering body. This is called the Rayleigh approximation. For an arbitrary body, the backscatter cross section is given by Ruck, et al., 1970.

$$\sigma = A_0 V^2/\lambda^4$$

Where λ is the radar wavelength, V is the body volume, and A_0 is a parameter that depends on the body shape, body material, and incident field polarization. In the case of a dielectric sphere

$$A_0 = 36\pi^3 \left|\frac{\epsilon - 1}{\epsilon + 2}\right|^2$$

The Rayleigh approximation is usually valid for bodies of dimensions less than one tenth of the radar wavelength.

At the other extreme, for a radar wavelength much smaller than the body dimensions, the theories discussed in the previ-

ous section (i.e., rough surfaces) can be applied here if we take into account the average curvature. In the case of a smooth sphere, the backscatter cross-section is

$$\sigma = \pi a^2 \left| \frac{\epsilon - 1}{\epsilon + 1} \right|^2$$

The general behavior of σ at different frequencies is sketched in Fig. 11. In the case of actual geological surfaces, such as the fans in Death Valley, the best we can expect at the present time is some conclusions about the gross characteristics of the radar images. In the case of small-size gravel (less than few centimeters in size), the X-band imagery should be appreciably brighter than the L-band imagery because of the fourth law dependence. However, for the same reason, the L-band imagery brightness is more sensitive to variation in the gravel-size distribution.

In the case of backscatter from spherical bodies, there is no depolarization for a linearly polarized incident wave. Therefore, if we neglect multiple scattering (this will be discussed later), the cross-polarized image of a field of spherical gravel will have very low brightness.

The depolarized backscatter from several types of scatterers (elliptical disk, elliptical cylinder, parabolic cylinder, spheroid) was studied by Chytil (see Beckmann, 1968). His results are summarized as follows:

(1) The depolarization factor is approximately proportional to $\alpha(a/\lambda)^{-4}$ where α is a small (i.e., $\lesssim 1.5\lambda$) constant factor.

(2) For surfaces having no edges, the depolarization is less than 10^{-2} for $a \gtrsim 1.6\lambda$.

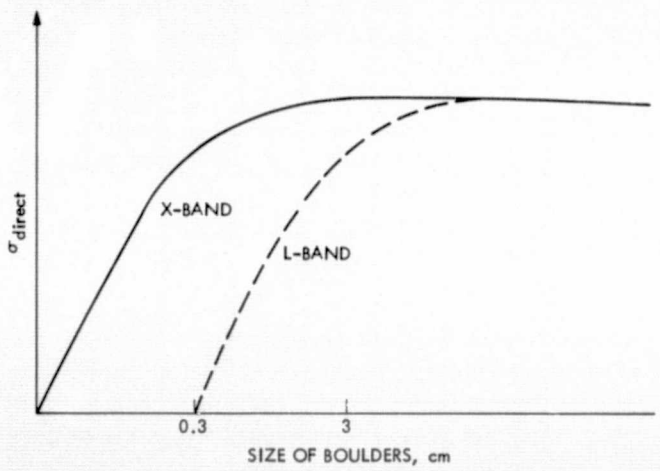

Fig. 11. Sketch of the behavior of the mean backscatter cross section from boulders at X-band and L-band

Also of interest is the depolarization due to edges. An edge will backscatter only if it runs perpendicular to the direction of incidence (Beckmann, 1968). Also, except in very special cases, it does not depolarize the linearly incident wave.

The situation becomes more complicated in the case of gravel fields, such as the one shown in Fig. 7d. Both the rough surface models and the finite-shaped bodies models must be considered in trying to understand the behavior of the backscattered radiation. In general, we can expect that the direct and cross-polarization imagery will have low brightness at wavelengths appreciably longer than the average size of the gravel. At wavelengths of the same order as the gravel size there will be strong direct backscatter because of the Bragg resonance effect as well as scattering from individual rocks. At shorter wavelengths, the image brightness will level off because of the scattering from individual rocks. This behavior is sketched qualitatively in Fig. 11.

Twersky (see Beckmann, 1968) studied the case of randomly spaced, perfectly conducting hemispheres on a conducting plane. He assumed that the wavelength is small relative to the average separation between the hemispheres. This model takes into account all of the multiple interaction phenomena at near grazing angles (i.e., shadowing, multiple reflection). Based on this model, he concluded that the scale of the roughness does not affect the angular dependence of the backscatter concentration and σ_{VV} always decreases at a slower rate than σ_{HH}.

The effect of multiple scattering is especially important in the case of dense concentrations of scatterers. Multiple scattering affects mostly the behavior of the cross-polarized component. In the case of spherical scatterers, there is no backscatter depolarization of the singly scattered linear incident waves. However, a depolarized component exists if the wave is doubly or multiply scattered (see, for instance, Beckmann, 1968; Pollack and Whitehill, 1972). In the case of elongated or nonspherical scatterers, both single and multiple scattering would lead to depolarization. If we consider the behavior, as a function of frequency, of the ratio of cross-polarization over the direct polarized component, we expect that in the case of single scattering this ratio should stay relatively constant, because it depends mostly on the shape of the scatterer. However, if the depolarized component is mostly a result of multiple scattering, the ratio should decrease as the wavelength increases beyond the scatterer size. This is a result of the fact that scattering is the cumulative product of many single scatterings which, in turn, decrease as a function of the fourth power of radar wavelength.

The above effect is consistent with the results of Pollack and Whitehill (1972) who studied the multiple scattering

effects of volume scatterers on the radar echo from the Moon. They concluded that volumetric multiple scattering can account for at least half of the observed depolarization and that the ratio of the polarized to depolarized radiation changes little as a function of frequency for wavelengths shorter than the average size of the scatterers.

Subsurface single and multiple scattering must also be accounted for in studying radar images of the Earth's surface. However, because of the relatively high microwave losses (as a result of moisture) in the material in the upper layer of the Earth's surface, the following behavior is expected:

(1) Except in extremely dry or permafrost regions, subsurface scattering will have little effect on X-band radar imagery, because the radiation will penetrate less than a few centimeters through the surface layer.

(2) As the wavelength increases, more and more penetration occurs. As a general rule of thumb, the penetration depth does not usually exceed a few radar wavelengths.

(3) In regions with high moisture, the penetration depth is practically negligible at all wavelengths commonly used in radar imaging.

These different behaviors allow us to sketch the way the ratio $\sigma_{cross}/\sigma_{direct}$ behaves as a function of frequency for volumetric multiple scattering (see Fig. 12).

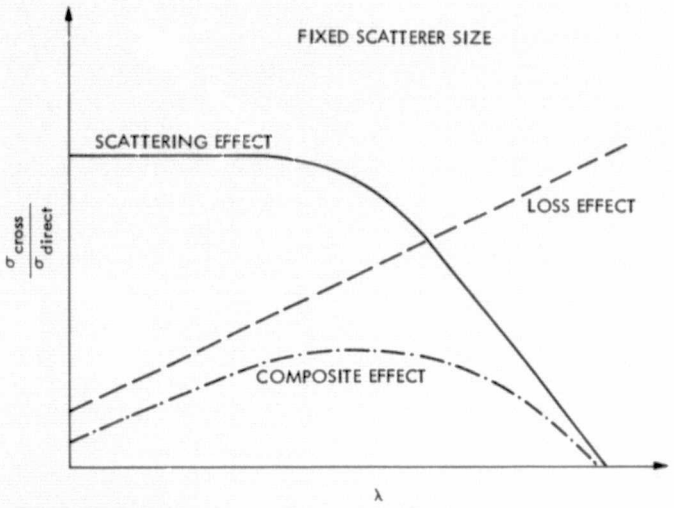

Fig. 12. Behavior of the ratio of $\sigma_{cross}/\sigma_{direct}$ for scattering from subsurface scatterers. As λ increases, the absorption loss decreases, leading to a lower loss in the multiple scattered wave. At the same time, the scattering from each scatterer decreases, leading to faster fall of the cross-polarized component

In summary, we can make the following conclusions, which could help in analyzing radar imagery of geologic surfaces where scattering from finite shaped bodies plays a major role:

(1) Scattering from gravel of a size much less than the observing wavelength is governed by a fourth-power law (i.e., $\sigma \sim (a/\lambda)^4$). Usually the imagery is brighter at shorter radar wavelengths. Comparison of imagery taken at a large number of different frequencies (i.e., spectrometric radar imaging) would allow the derivation of gravel size distribution.

(2) Spherically shaped gravel does not depolarize, unless it is relatively densely spaced, giving appreciable multiple scattering. Nonspherical gravel will always depolarize; however, single scattering depolarization is usually weak.

(3) The ratio of the cross-polarized image to a direct polarized image is constant as a function of frequency when multiple scattering is negligible. If this ratio decreases as the wavelength changes, then multiple scattering is important. If this ratio increases and then decreases as the wavelength changes, then subsurface multiple scattering is also involved.

D. Overall Summary of General Properties of Radar Imagery

In the previous subsections we stated a number of hypotheses that could be used to derive information on the surface geology using multispectral multipolarization radar imagery. It is clear that the use of ratioing techniques could appreciably help in the interpretation of radar images. It is also clear that simple analysis of the brightness of radar images or radar ratio images is not sufficient by itself. This type of analysis has to be combined with the usual photogeology analysis of patterns on the image that allows distinguishing the characteristics of the surface. These two types of complementary information in the radar images could then be used in conjunction with imagery from other sensors (i.e., IR imagery, visible imagery) as well as spotcheck ground truth (if possible) to understand the surface characteristics.

E. Radar Response to Surface Materials in Death Valley

Surface materials in Death Valley include alluvial fan deposits and evaporites. Units defined by Hunt and Mabey (1966) are distinguished primarily on the basis of composition and surface texture, ranging from smooth silty playas to rough eroded salt. Because of the strong dependence of electromagnetic wave scattering on roughness on the scale of one wavelength, the radar systems employed in this study – L-band

(25 cm wavelength) and X-band (3-cm wavelength) – are most sensitive to roughness variations in the range of a few millimeters to a few decimeters. We adopt the convention of referring to the surficial units by their map symbols.

Surface photographs referred to are indexed on Fig. 13.

1. Qg_2

The oldest of the exposed fan gravels (Qg_2) forms flat surfaces of nondeposition. Although surfaces of this age contain more boulders than do younger units, the processes of deflation and creep have yielded a smooth desert pavement

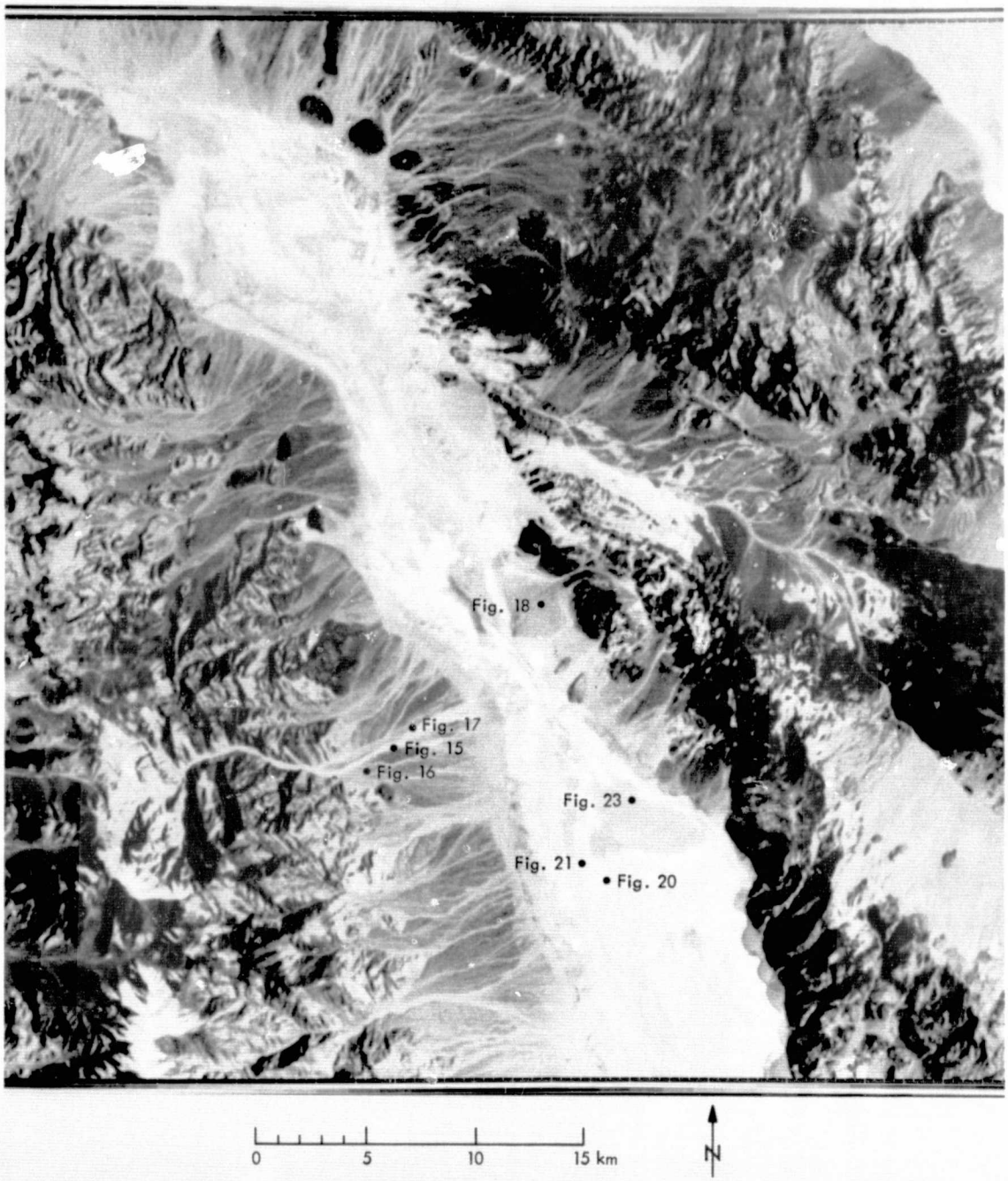

Fig. 13. Portion of LANDSAT frame 5367-17134 with surface photo locations indicated

composed of an interlocking mosaic of subangular rock fragments. Particle sizes range from partially buried boulders to sand, finer-grained surficial materials having been removed by deflation.

The fragments on the No. 2 gravel surfaces are the most angular of the alluvial materials. Formerly rounded boulders, cobbles, and pebbles have disintegrated *in situ*, leaving heaps of angular blocks, slabs, and flakes (Fig. 14). Typically seventy-five percent of the boulders have lost their roundness, with disintegration most thorough near the salt pans.

L-band radar return from Qg_2 is comparatively low in both polarizations and appears to be dominated by returns from widely spaced angular blocks and slabs, the pavement in general, being smooth to this wavelength. As seen on the LVV/LVH ratio image (Fig. 15b), this surface yields a depolarized component that is small compared to other smooth units. Weak depolarized returns have been observed from several rock types by Cooper (1966) and Gillerman (1967). McCauley (1972) classified the occurrences and offered a physical explanation for them. All anomalies were found on K-band (0.86 cm) dual-polarization (HH and HV) data and were marked by strong HH returns and weak HV returns. Rock types included recent lava flows, some Tertiary volcanics, and certain massive sandstones.

The physical explanation advanced for the anomalously low cross-polarized return was specular nondepolarized reflection from planar rock surfaces. In detail, McCauley could account for this specular reflection in terms of the outcrop's small-scale morphology:

(1) The recent lavas are blocky as a result of their eruption. Such blockiness is especially well developed in viscous lavas such as rhyolites and dacites. The surface is dominated by planar surfaces that are much larger than the wavelength of the radar.

(2) The older lavas have acquired a blockiness from weathering and development of rubble. Such a surface would be found where dryness prevents the formation of a soil or vegetation cover.

(3) The massive sandstones (Aztec, Navajo) weather to bare smoothly rounded forms having limited specular areas. Because the spacing of the boulders is similar to the resolution of the radar, the imagery has a speckled appearance.

Fig. 14. Oldest fan gravel (Qg_2). Scale is 18 cm. Surface is desert pavement, a smooth interlocking mosaic of varnished angular flakes littered with 10– 30–cm slabs. The mosaic is transitionally rough to X-band, while specular nonpolarized returns from the sparse population of slabs accounts for the L-band brightness

Fig. 15a. Portion of LANDSAT frame 5367-17134 with LHH radar imagery inserted

FOLDOUT FRAME 2

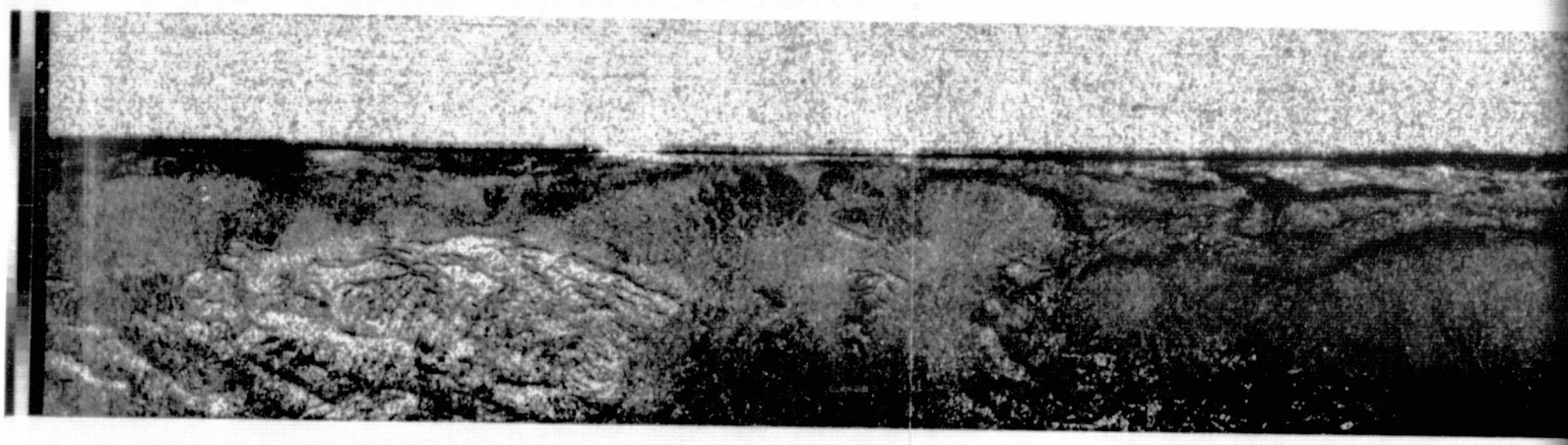

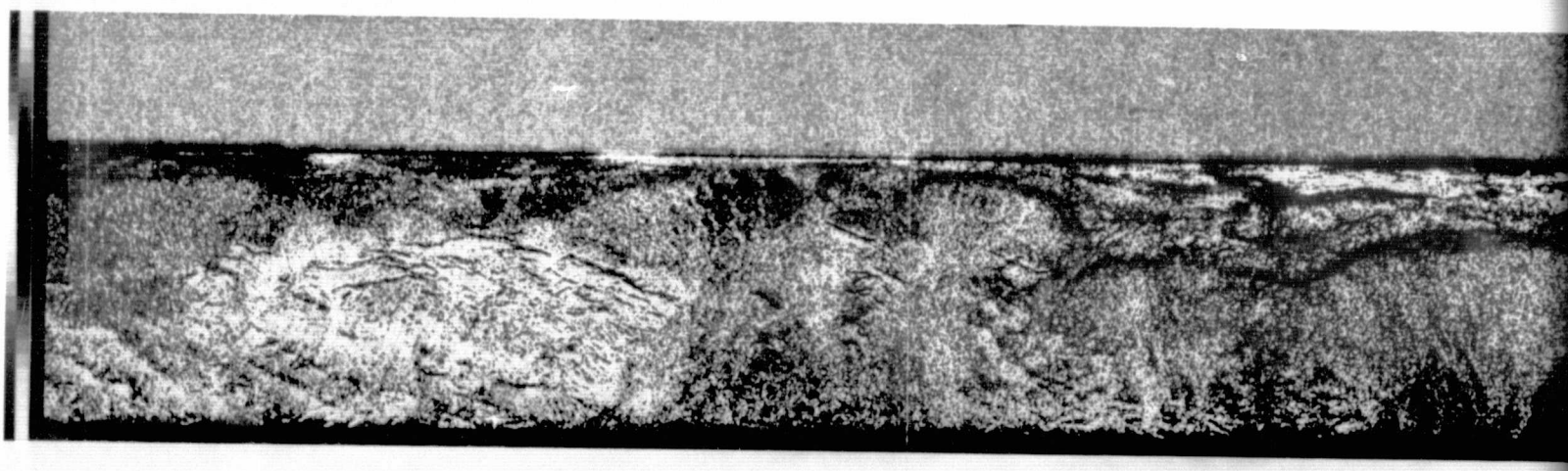

FOLDOUT FRAME 3

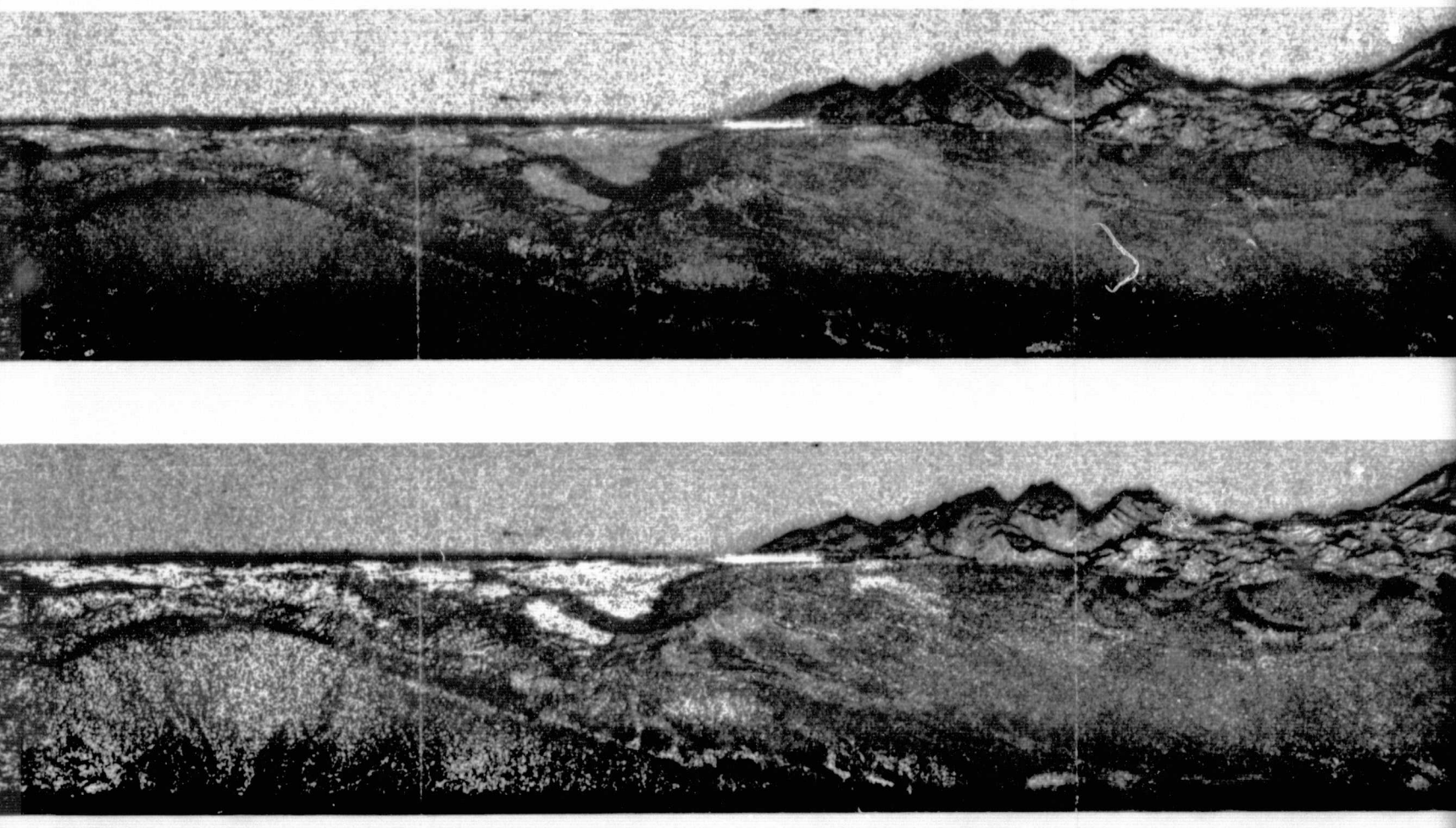

Fig. 15b. LVH/LVV ratio image (upper); LVH-LVV dif

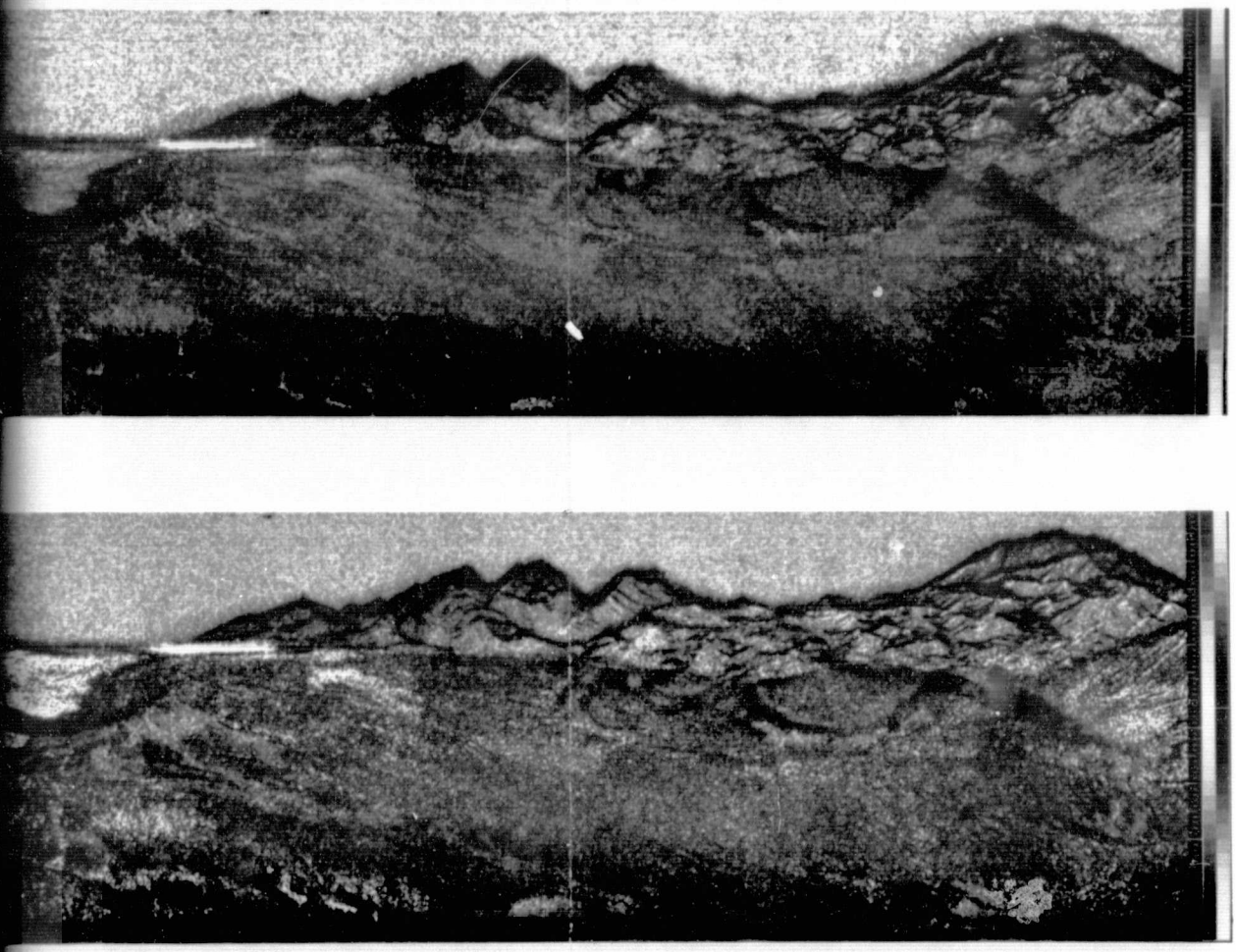

Fig. 15b. LVH/LVV ratio image (upper); LVH-LVV difference image (lower)

In the Death Valley test site, the desert pavements show somewhat different characteristics from the examples above:

(1) Planar faces are nearly the same scale as the radar wavelength.

(2) The targets are more widely spaced than are the outcropping blocks described by McCauley (1972).

As a consequence, the like-polarized (LVV) return is rather weak and the contrast between polarizations suppressed.

The X-band image (Fig. 4a) shows Qg_2 as a rather poor scatterer at 3 cm. The LVV/XHH ratio image, however, indicates that the pavement is a significantly rougher surface to X-band than to L-band. Since the planar specular targets are comparable in size to the larger of the two wavelengths used in this study, these targets have a constant scattering cross-section at both wavelengths and the additional brightness of Qg_2 at 3 cm must be the result of scattering from the pavement itself. Figure 16 shows that the desert pavement does have roughness on the scale of several millimeters.

In a multifrequency study of alluvial fans near Pisgah Crater, Dellwig (1969) found a large difference in return between K_a-band (λ = 0.84 cm) and P-band (70 cm) imagery. The fan is covered with basalt fragments, 85% of which are less than 5.1 cm and 75% of which are less than 2.5 cm. Since the region of strong Rayleigh scattering for P-band ($\lambda/10$ = 7 cm) is well above the average roughness, theory is in agreement with the observation of low scattering at P-band.

The roughness on the pavements in Death Valley is bimodal, with millimeter-sized features characterizing the pavements as a whole and with widely spaced decimeter-scale slabs and blocks accounting for a majority of the roughness seen at longer wavelengths.

2. Qg_{3-4}

The younger fan gravels (Qg_3 and Qg_4) form surfaces and channels currently undergoing erosion and deposition. Both are fairly well stratified in coarse and fine layers and have fewer boulders than does Qg_2. Qg_3 is a transportation unit, representing gravel and cobbles in transit downfan from the bedrock sources. Qg_4 is generated by processes on the fan, primarily by reworking of Qg_2 and Qg_3 by torrential rains.

Both of the active fan gravel units have high gravel/sand ratios and are somewhat better sorted than is Qg_2. They are considerably rougher than the pavement, "because the ill-sorted small boulders, cobbles, and pebbles stand at different heights and are distributed irregularly on the surface" (Hunt and Mabey, 1966).

Fig. 16. Desert pavement under low sun angle illumination. Scale of roughness of millimeters. Scale bar is 20 cm

Qg_3 and Qg_4 have considerably different hydrologic properties from Qg_2. The pavements are underlain by a poorly permeable silt layer that is overlain by a tightly interlocking mosaic of pebbles. This promotes runoff and thus seriously degrades ground water discharge. In contrast, the active fan surfaces are very rough and permeable to great depths and are therefore important in the hydrology of the Death Valley basin. The radar signatures of the active fan are distinctly different from those of the pavements. Using the system parameters of this study, however, Qg_3 and Qg_4 are not distinguishable on the west side of the Valley, since they differ but little in mean grain size, sorting, and angularity.

The rough, uniform surface of the active fan tends to scatter strongly at both X-band and L-band frequencies. Because of this the LVV/XHH ratio image shows a rather featureless grey tone and may be regarded as one of the few "normal" areas in the imaged region. Considering the scale of roughness seen in the field (Fig. 17), the active fan would be a

Fig. 17. Younger fan gravels (Qg_3). Scale is 18 cm. Surface partly composed of coarse sand and gravel, partly of subangular to subrounded cobbles and boulders. A strong scatterer at both radar frequencies. Comparatively dense population of multiple scatterers (cobble size most favorable) assures a substantial depolarized return from this surface. Youngest channels (Qg_4) distinguishable from Qg_3 in the field by morphology and lack of varnish rather than by roughness

strong scatterer at wavelengths from K-band (0.84 cm) to P-band (70 cm). A comparison with the Pisgah fans demonstrates that important differences in fan roughness exist in the semiarid to arid regions of the southwestern United States. Such variations in roughness have been observed on a variety of fans by these authors (unpublished data) and appear to reflect differences in source lithology, slope, climate, and tectonic history.

An excellent example of the effect of source lithology occurs outside the prime imaging site in Death Valley. Small fans on the east side of the valley drain outcrops of Tertiary playa sediments and volcanic rocks. The surfaces of these fans are much smoother than those of the west side fans; the cover being coarse sand with a sparse population of cobbles (Fig. 18). The L-band imagery (Fig. 19) shows the surfaces as completely dark, except for the moderately bright surface of the Furnace Creek fan.

In contrast, X-band imagery of the east side fans shows a wealth of detail:

(1) The Furnace Creek fan has X-band roughness similar to the bouldery west side fans.

(2) Substantial portions of the upper reaches of the other east side fans are also very bright.

(3) Qg_3 and Qg_4 are distinguishable locally, with the braided Qg_4 deposits showing dark. The higher resolution of the X-band system is clearly advantageous in discerning the intricate drainage patterns on the fans.

Depolarization by the active fan surfaces also tends to be uniform and of intermediate value. Physically, the depolarization of radar by the moderately rough gravel surfaces appears "normal" compared with the behavior of the specular targets of the pavements or the peculiar cavity effects of the salt units (described below). The physical model most appropriate for describing the depolarization by the active fan segments is one involving multiple reflections from the densely packed population of cobbles and boulders.

3. Qf

The floodplain deposits (Qf) are widespread and extremely variable in surface character. Qf consists of salts and saline muds primarily deposited by seasonal flooding. The lowest portions of the floodplain are covered by a coating of nearly pure salt deposited by evaporation of water supplied by sheet flooding and capillary rise of groundwater. Elsewhere on the floodplain, slightly higher areas are swept clean of salt by sheetflooding (and eolian action); there saline muds are exposed at the surface.

The floodplain is everywhere a very smooth surface, the only noticeable relief being centimeter-scale nodular bumps (Fig. 20) and the upturned edges of meter-scale desiccation polygons (Fig. 21). Contrary to expectations, the radar brightness of Qf is not the uniform darkness expected of a specular surface. Instead, substantial fractions of the floodplain surface span nearly the entire range of brightness on imagery in all radar configurations, and there is less than perfect correlation among the data sets at a given point. In general, however, the floodplain appears brighter in the like-polarized L-band imagery than in the cross-polarized L-band or the like-polarized X-band data. This situation is clearly anomalous,

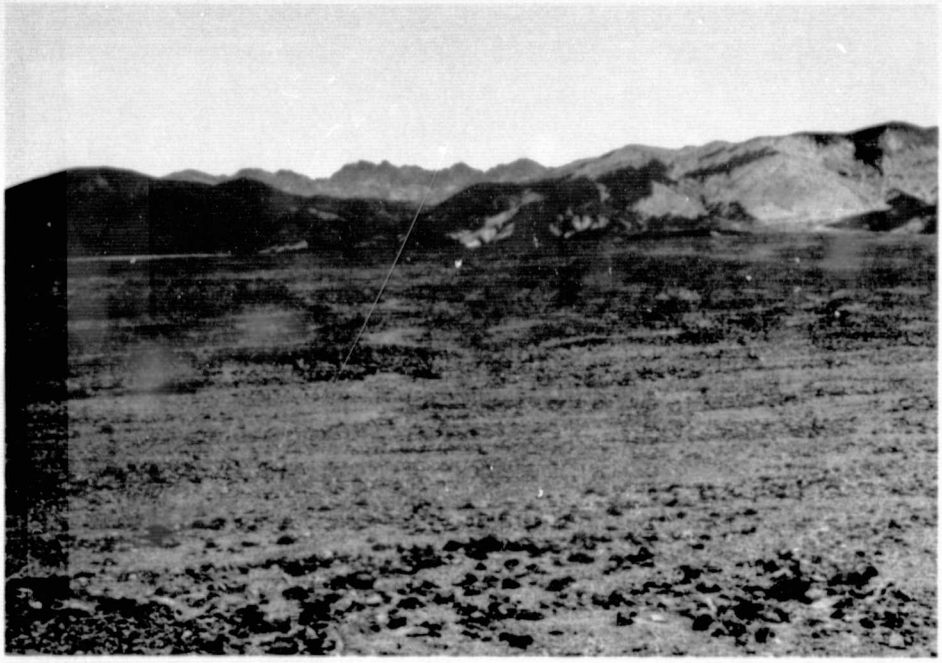

Fig. 18. Younger fan gravels (Qg_{3-4}) on east side of Valley. Source lithology (playa sediments and volcanics) yields coarse sand and gravel. Surface is moderately strong X-band scatterer, but is very dark on L-band imagery. Polarization properties are unknown as imagery of this area was not computer processed. Compare this surface with the bimodal size distribution on Qg_2 (Fig. 15)

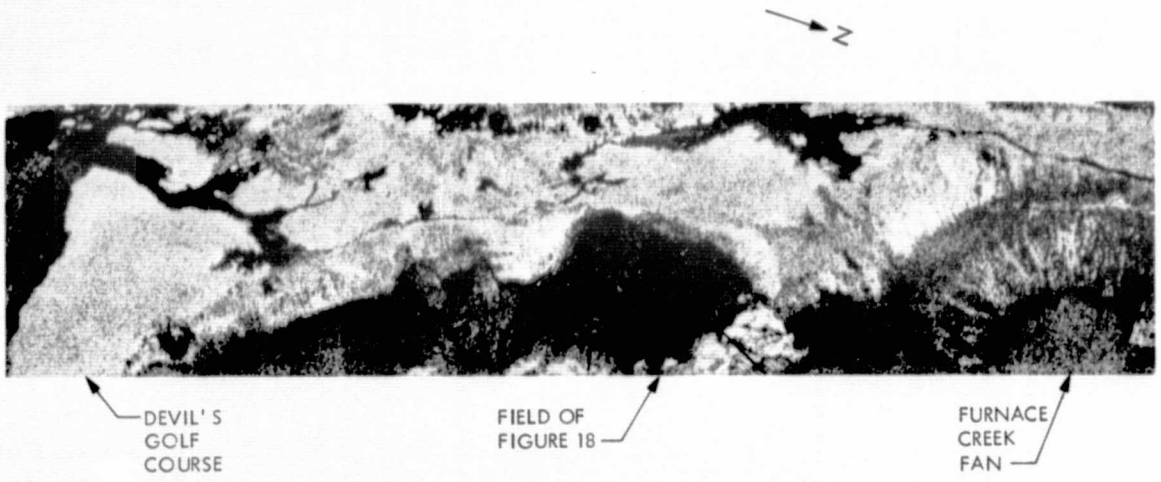

Fig. 19. L-band (25 cm) radar image including the east side of Death Valley. Note the dark lobes including and adjoining the field of Fig. 18. This image was not included in the computer processing

Fig. 20. Floodplain unit (Qf). Over much of the surface the only microrelief is in the form of centimeter-scale nodular bumps. Although the roughness of this type of surface is similar to that of the pavements (Qg_2), much of the floodplain is very bright at X-band. This and the anomalous brightness at L-band provide a strong argument for microwave penetration

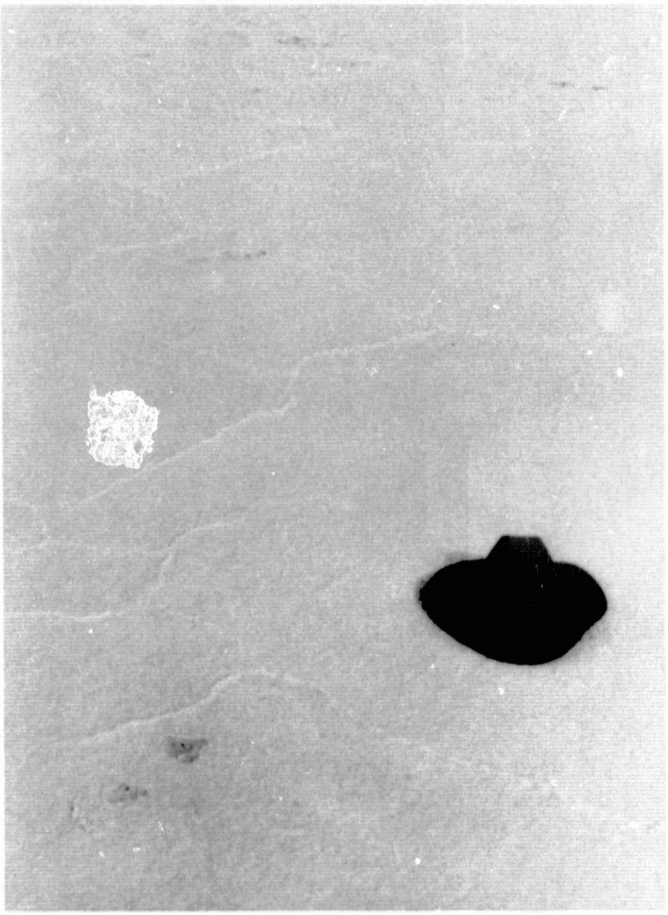

Fig. 21. Edges of desiccation polygons on Qf. These small-scale ridges are so widely spaced ($>$ 1 m) that they are unlikely to contribute significantly to radar return

especially with regard to the frequency effects. The most obvious explanation, and the one adopted here, is that some penetration of the surface by the L-band radar has occurred. Theory predicts (see Section IV-D) that the VV configuration of the L-band radar used in this study should be particularly sensitive to dielectric contrasts at depths of the order of one wavelength (25 cm). Field data was not taken at the same time as the data acquisition, but insofar as the surface and subsurface conditions remain stable in such an arid environment, field data taken a year later should provide some information on such an electrical discontinuity. Our limited investigation of the floodplain surface indicates that such an electrical contrast, in the form of a shallow brine aquifer, does exist at variable depths on the floodplain. Locally, this aquifer intersects the surface and is marked by a damp, slippery layer of salty mud. Electrically, such an area will behave as a single layer and will appear as a specular reflector. Elsewhere, however, the brine layer is separated from the soil-air interface by a capillary zone having considerable lateral variation in permeability. Such a heterogeneous vadose zone provides a second underlying scatterer. Locally, mounds and root systems associated with phreatophytes contribute to scattering.

The low brightness of the X-band image of Qf compared to the L-band (VV) data may result from some combination of three effects:

(1) Less penetration

(2) Less favorable polarization configuration (XHH)

(3) Temporal effects (see below)

Qf is the only unit in Death Valley displaying significant temporal variation in radar brightness (Fig. 22). In contrast to the floodplain deposits of Badwater Basin, Qf in Middle Basin and Cottonball Basin behaves as a rather monotonous specular surface on all three radar configurations.

4. Qh

The extremely rough salt of the Devil's Golf Course (Qh) is one of the strongest scatterers in the Valley. Chemically, this unit is composed of nearly pure salt, about 95 percent sodium chloride, with subordinate chlorides of calcium, magnesium, and potassium. The surface (Fig. 23) consists of jagged pinnacles 15 to 25 cm wide and 0.3 to 0.7 m high separated by depressions 0.3 to 0.7 m wide. Such a dense array of pyramidal or conical forms has numerous surfaces normal to an incident radar beam for look angles employed in this study (20 to 55 deg). This geometry, plus the presence of fine-scale roughness on the pinnacles, imply that Qh should behave as a nearly isotropic scatterer to wavelengths less than several meters.

The most outstanding property of Qh, however, is visible in the polarization ratio image (Fig. 15b). Qh is everywhere a powerful depolarizer, as would be expected for such a densely populated field of multiple scatterers.

5. Qhr

The rough silty rock salt unit (Qhr) is peripheral to and in gradational contact with Qh. It has 20 to 40 percent silt admixed with massive salt over most of its outcrop and is closely similar to Qh in size and spacing of pinnacles and in micro-relief features. Like Qh, it is a strong scatterer, although locally the X-band image shows Qhr slightly darker than Qh. The cause of this minor anomalous behavior has not been determined.

6. Qhs

The smooth silty rock salt (Qhs) is a layered deposit consisting of 2 to 15 cm of brown silt underlain by about 0.3 m of silty rock salt.

Although termed "smooth," Qhs is generally a strong scatterer at both frequencies. The important exception to this is the exposure near Badwater Basin. There, like the adjacent occurrences of Qf, Qhs has a variable, mottled appearance and, locally, the X-band image is darker than the L-band image. It appears likely that penetration effects are important here. For Qhs, the second reflecting boundary is the contact between silt ($\epsilon \cong 3$) and the underlying silty salt ($\epsilon \cong 8$). The silt thickness (2-15 cm) is quite reasonable for a multilayer model.

Although Qhs is a comparatively strong scatterer, it is readily distinguishable from Qh and Qhr on the polarization ratio image. The most likely physical explanation for the radar observations is that, for Qhs, scattering by subsurface features dominates the LVV return.

Figure 24 is a qualitative cluster diagram depicting the discrimination of geologic units by use of the three radar configurations. Brightness was estimated by eye on each of three images (VH, VH/VV, and VH/X) and compared to the geologic units shown on the maps of Hunt and Mabey (1966).

7. Summary

(1) Desert pavement (Qg_2) is distinguishable from the active fan surfaces (Qg_3 and Qg_4) in both frequency and polarization.

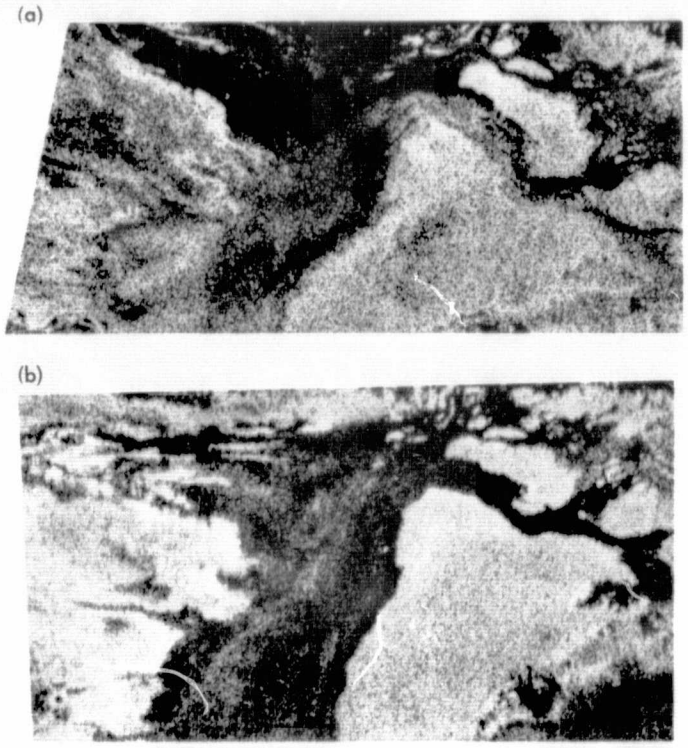

Fig. 22. Parts (a) and (b) show two L-Band (25 cm) images of the floodplain deposits near the Devil's Golf Course, showing temporal effects

Fig. 23. Rough salt (Qh). Jagged, intricately textured towers and mounds of nearly pure salt. Scale in foreground is 20 cm

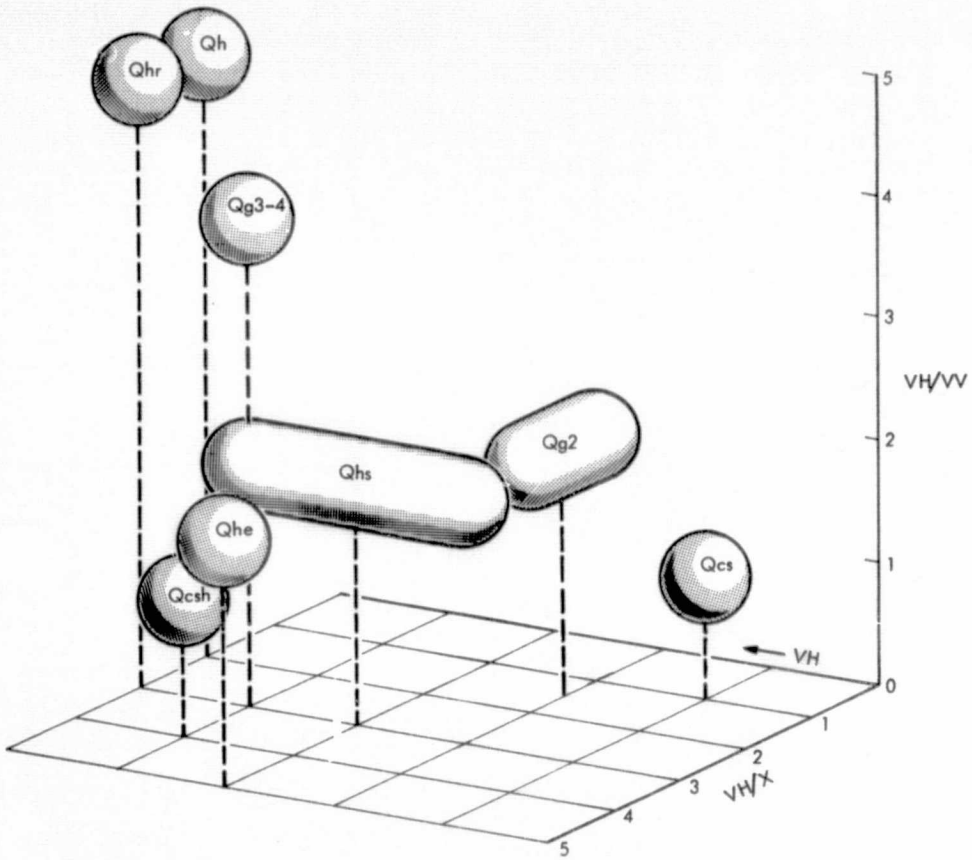

Fig. 24. Cluster diagram illustrating the image brightnesses of eight quaternary geologic units on one single-configuration image (LVH) and two stretched ratio images (LVH/XHH and LVH/LVV). "Balloons" are tethered to the lower plane for clarity (see text)

(2) Radar backscatter data demonstrates that Qg_3 and Qg_4 have different size distributions on opposite sides of the Valley. This is clearly a lithologic effect, with the Tertiary playa and volcanic rocks of the Black Mountains yielding much finer alluvium than the metamorphic rocks of the Panamints.

(3) The two rough salt units (Qh and Qhr) are distinguishable from other units in the Valley by their powerful depolarized returns.

(4) Moderately smooth surfaces such as Qg_2 and Qcs (basal sand facies) show clear frequency effects, X-band radar scattering more strongly.

(5) Tone reversals on multifrequency radar imagery of the floodplain (Qf) and smooth salt facies (Qhs) indicate penetration by the L-band radar.

(6) Several different radar scattering mechanisms are observed:

(a) Specular reflection (Qf)

(b) Non-depolarized specular reflection from facets (Qg_2)

(c) Multiple scattering (Qg_{3-4}, Qh, Qhr)

(d) Penetration and scattering from the water table (Qf) and from a lithologic boundary (Qhs)

(7) The use of computer-generated ratio and difference images allows the geologist to discern subtle brightness anomalies.

(8) Use of the three radar data sets (XHH, LVV, and LVH) achieves a nearly complete separation of the Quaternary geologic units in Death Valley (Fig. 25)

(9) Of the three possible two-channel combinations, use of the dual-polarization (VV and VH L-band) configurations is the most effective for rock-type discrimination. This is the simplest from the hardware standpoint, requiring only a single transmitter.

V. Synergism Effects

The technique for digital registration of LANDSAT and radar images is discussed in Section VII of this paper. Interpretation of the registered data set will be the subject of this section.

Combination of radar and LANDSAT imagery has been achieved by Harris and Graham (1976). Employing photographic techniques only, they made various color composites using four different techniques. These were additive as well as multiplicative techniques accomplished through the use of many internegatives exposed through different color filters.

The method with the most promise, they concluded, was an additive process involving the use of six negatives; three from LANDSAT MSS bands 4, 5, and 7 and three of the radar image. Each LANDSAT image was exposed through a different filter onto the color composite negative. In addition, the radar image was also exposed through each of the three filters (Fig. 26a). This method produced images that retained LANDSAT information in the radar shadows and simultaneously displayed both data sets elsewhere. Harris and Graham's (1976) purpose was to use LANDSAT imagery to identify surface types and radar imagery to define boundaries and portray relief. The higher resolution of their radar imagery (about 10 m) added more information as well.

One method not thought very useful by Harris and Graham (1976) consisted of a color composite formed from two of the four LANDSAT MSS bands with a radar image as the third component. Their objections to this technique were that only arbitrary colors could be assigned to the three component images and that radar, being sensitive to terrain slope, could alter color balance in the image even though spectral reflectivity in the MSS wavelength range did not change. Those features of this technique, however, seem desirable for maximum utilization of radar information.

The purpose of the work reported here, involving the use of digitally registered radar and LANDSAT imagery, was to use LANDSAT imagery as a base for registration of radar images of different polarizations and frequencies and as another dimension of imagery in the visible and near infrared regions of the spectrum. The method of digital image registration that was used involved the selection of tiepoints in both the master image (LANDSAT) and slave images (radar). The slave images were then manipulated so that their tiepoints coincided with the master tiepoints. This method is more fully explained in Section VII.

Two methods of presenting the combined LANDSAT and radar imagery were explored. The first involved the transformation of LANDSAT images from red-green-blue (RGB) color coordinates to hue-saturation-intensity (HSI) color coordinates. The hue and saturation components were then "stretched" to bring out subtle color differences. Finally, the digitally registered radar data were inserted as the intensity component and a color image was produced (Fig. 27). Details of the implementation of this method are contained in the

FOLDOUT FRAME 1

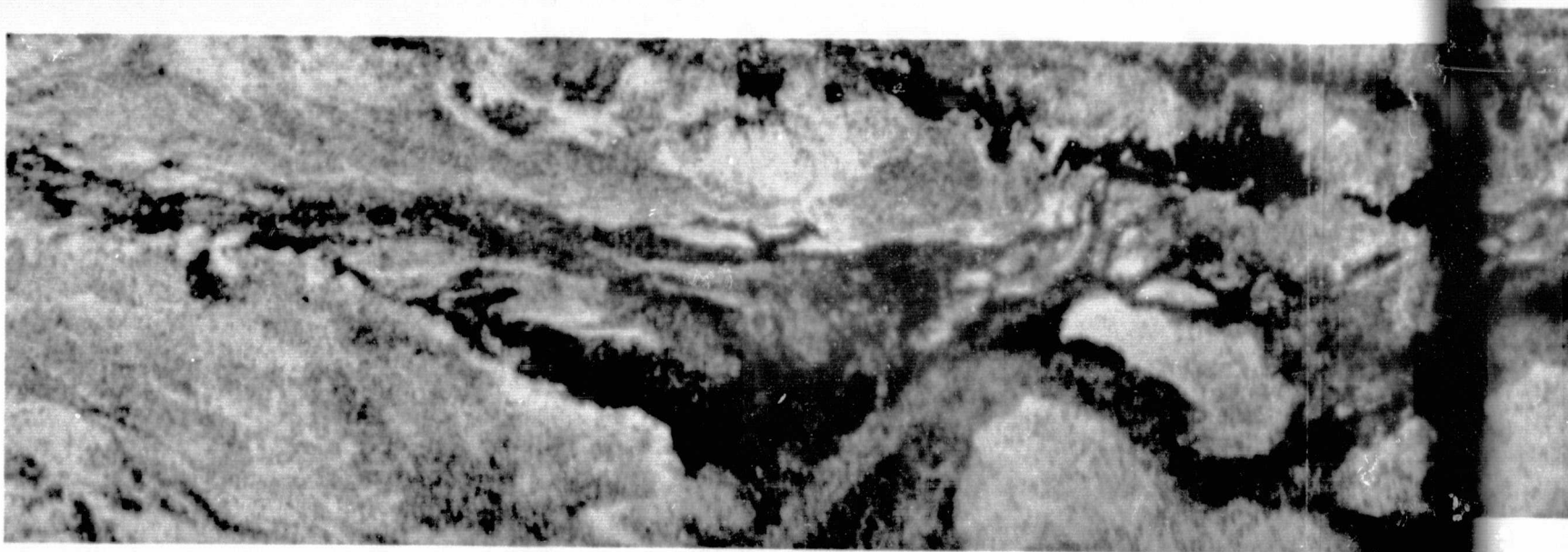

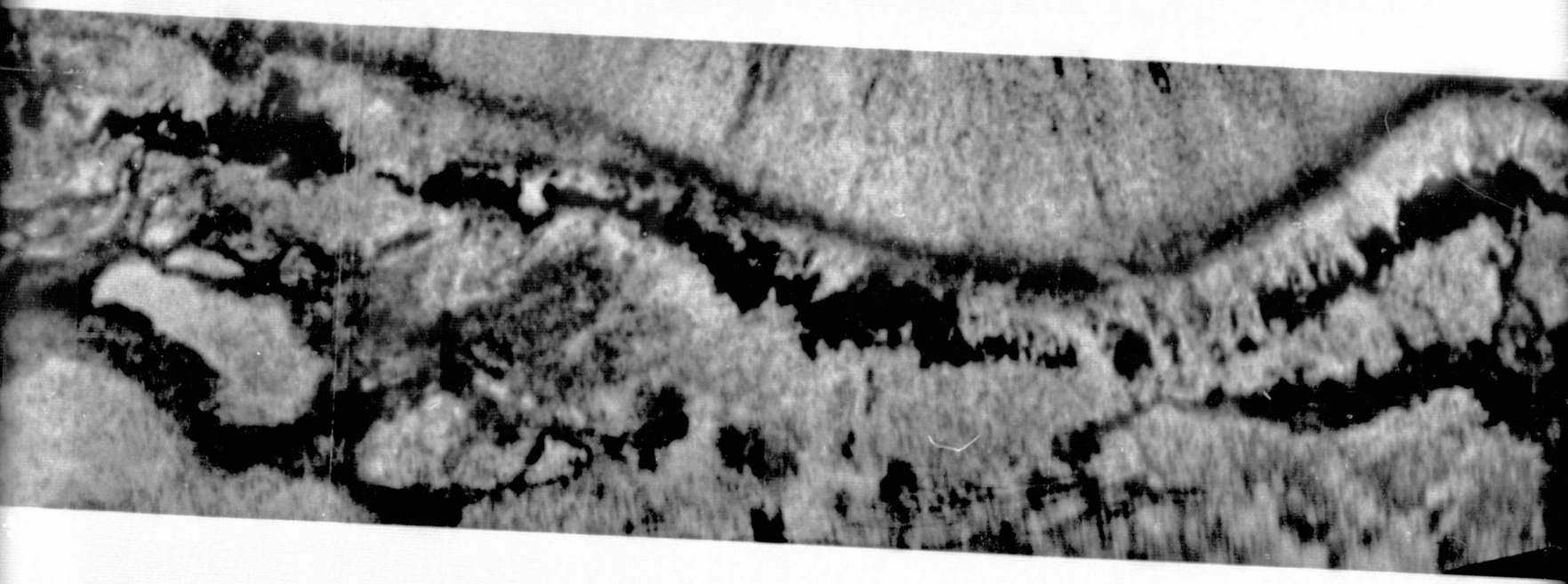

FOLDOUT FRAME 3

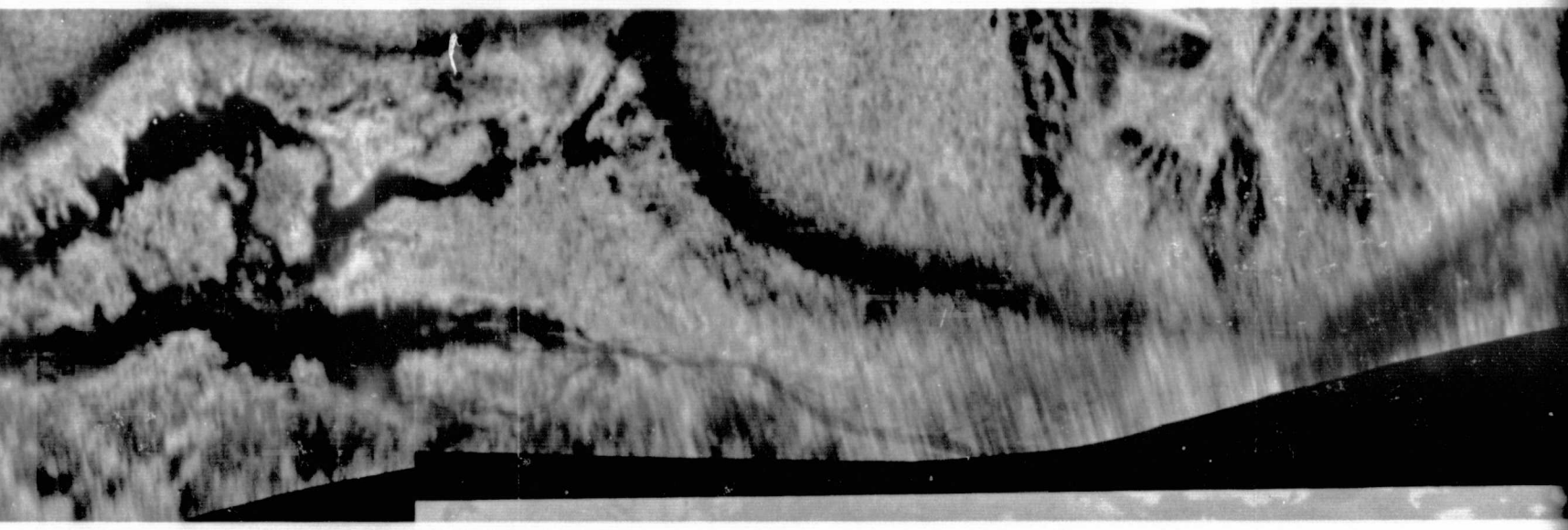

Fig. 25. Color-processed image combines the three registered radar data sets: red = L(V

ORIGINAL PAGE IS
OF POOR QUALITY

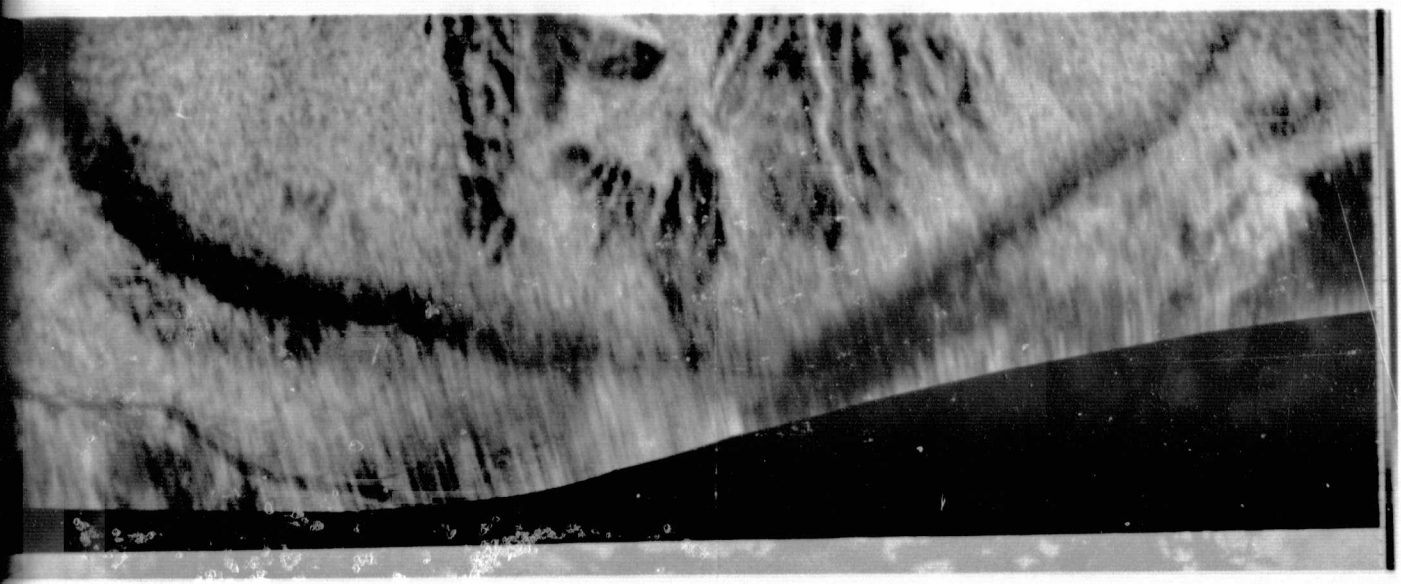

Fig. 25. Color-processed image combines the three registered radar data sets: red = L(VH), green = L(VV), blue = X(HH)

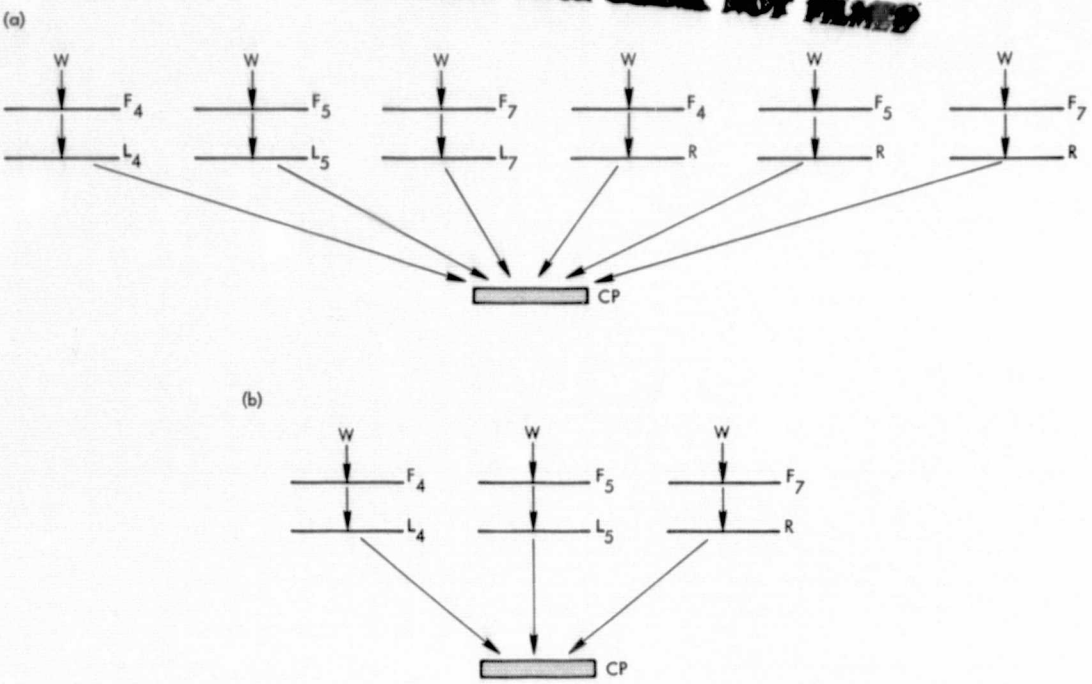

Fig. 26. Compositing techniques: (a) method 2 of Harris and Graham (1976), (b) method 4 of Harris and Graham (1976)

section on digital image processing. This method is similar to Harris and Graham's (1976) Method 2 in which the intensity information in their LANDSAT color composite was removed photographically, and a radar negative was used to supply the intensity (Fig. 26b).

The product of the intensity insertion method (Fig. 27) is difficult to interpret. Colors are ambiguous and appear saturated in many cases. The radar affects intensity as it should (see Badwater Basin), but features in the saltpan are, in many cases, obscured by colors. Plans exist to repeat this method using little or no hue and saturation "stretching" in order to evaluate the utility of radar intensity insertion without other processing. Much of what can be seen in Fig. 27 can also be seen in the color image (Fig. 1) produced by the second color composition method to be discussed.

The second technique yielded more interpretable imagery. Figure 1 shows the result of using a black-and-white LANDSAT intensity image as the red component, and VH and VV polarization L-band radar images as the green and blue components, respectively, of an RGB color composite. These two polarizations were acquired simultaneously on August 13, 1976 by the JPL L-band Synthetic Aperture Radar mounted on the NASA Convair CV-990 aircraft. The flight line was from northwest to southeast. This resulted in imagery illuminated from nearly the same direction as the basic LANDSAT image. The geometry of the JPL L-band radar is discussed in the introduction to this paper.

Several interesting observations can be made using the LANDSAT-radar false-color composite in Fig. 1. Details on the alluvial fans are more easily seen, differences in some of the evaporite units on the salt pan are apparent, and stronger topographic effects are evident, though topography is still a problem and causes some local registration errors. Some effects of dual-polarization radar can be seen in the composite, especially in the saltpan. These effects are treated more fully in Section IV-E.

The fact that LANDSAT can see differences in the amount of desert varnish on alluvial fan surfaces yet is insensitive to desert pavements, while L-band radar can easily discern desert pavements yet is blind to desert varnish, dictates the use of the two sensors to map the gravel units of Hunt and Mabey (1966). Their units Qg_2 (oldest), Qg_3, and Qg_4 (youngest) have been described in Section II of this report. The major means of distinguishing these units is by amount of desert varnish, roughness, and topographic context – all three of which are available in a LANDSAT-radar composite.

Trail Canyon fan is shown in detail in Fig. 28. Desert pavement areas are obvious as dark red elongated bodies extending radially from the apex of the fan. These areas are

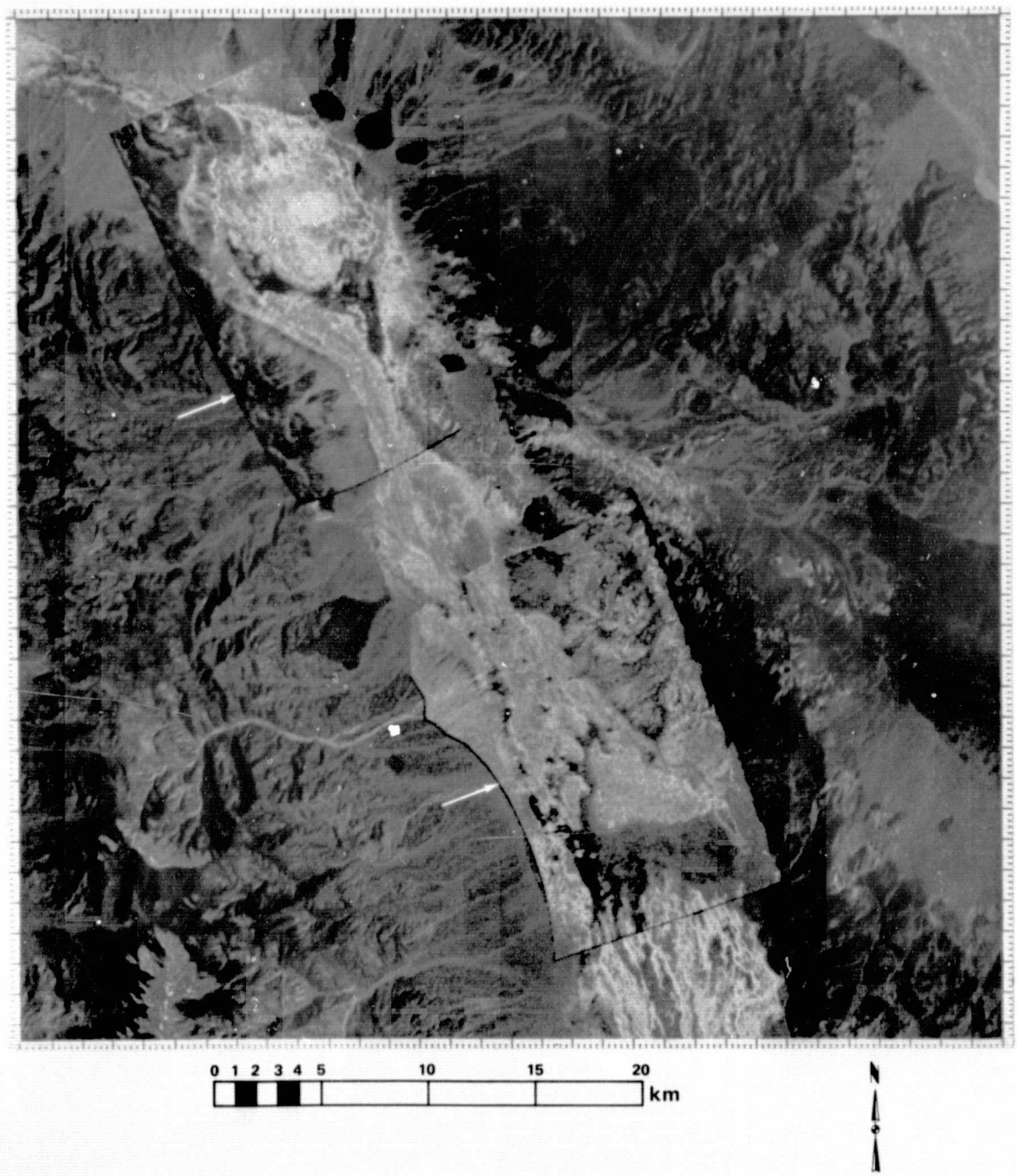

Fig. 27. Portion of LANDSAT frame 5367-17134 with hue and saturation stretching and two L-band radar images inserted as intensity (see arrows)

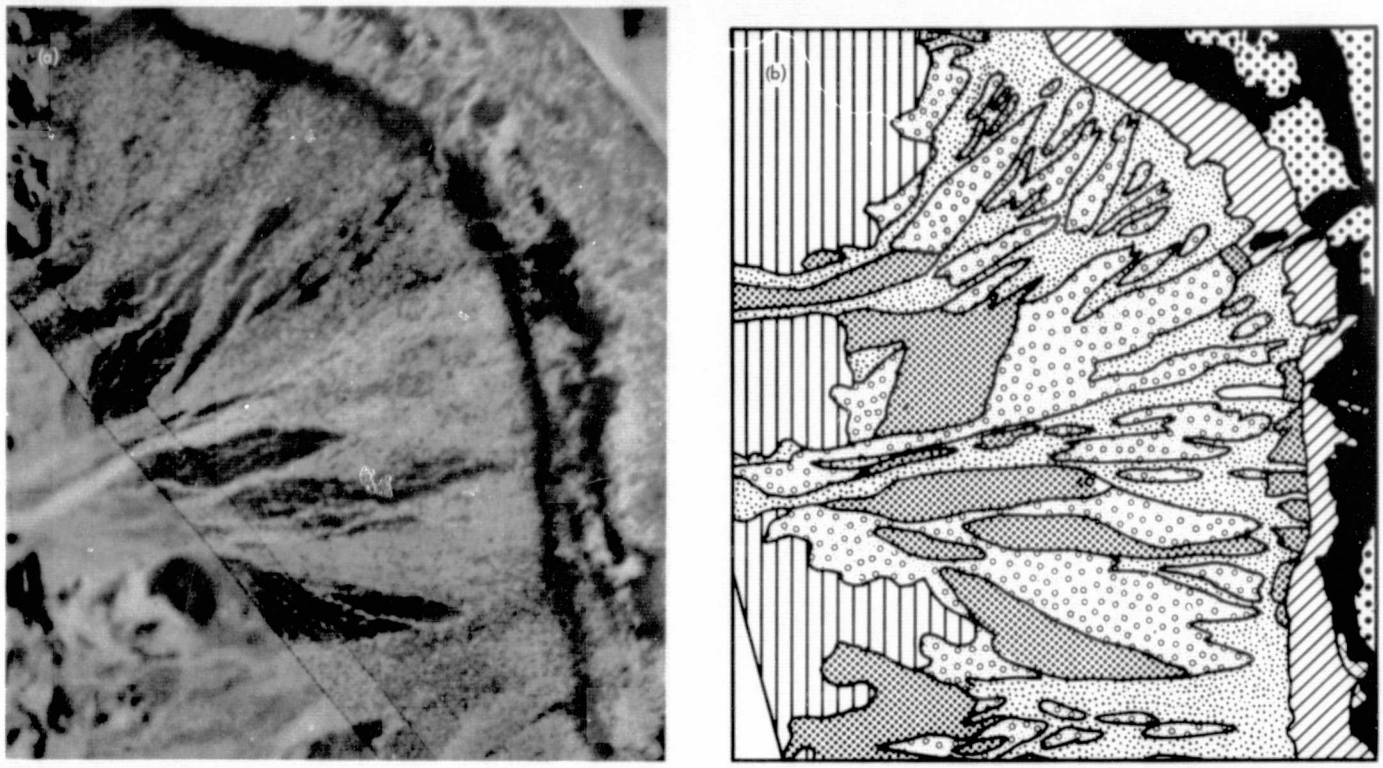

Fig. 28. Detail of Trail Canyon fan: (a) Portion of Fig. 1 showing Trail Canyon fan, (b) detail of geologic map of Fig. 4 showing Trail Canyon fan. Units are the same as Fig. 4.

shown on the geologic map of Hunt and Mabey (1966) (Fig. 28b) as Qg_2, the oldest gravel unit on the alluvial fans. They are dark red in the composite because of the large amount of desert varnish and the very smooth desert pavement on these old surfaces. Some return, though, is apparent from the LANDSAT image.

The next oldest gravel unit is Qg_3 and is depicted on the composite as a light blue-green. This unit has dark desert varnish but is rough to the L-band radar and therefore bright.

The youngest gravel unit, Qg_4, shows up light red or magenta in color indicating it is bright in all components. Since Qg_3 and Qg_4 appear the same in L-band imagery, the resolution of LANDSAT limits the resolution between Qg_3 and Qg_4.

Along the base of the fans is a band that appears very dark red. This indicates a return from LANDSAT but no return from L-band VH or VV polarizations. JPL L-band HH polarization radar imagery of the area at the base of the fans has been studied by Schaber, Berlin, and Brown (1976) who found a systematic decrease in grain size toward the foot of the fans. This grain size decrease passed through the Rayleigh criterion for specular reflection for L-band wavelengths at a fairly well-determined point in grain size producing a dark band in imagery at the foot of the fans. The higher albedo in LANDSAT imagery is the result of disintegration of rocks leading to little desert varnish at the foot of the fans.

Flood deposits in the southern part of Badwater Basin exhibit polarization effects. The color composite shows this area as red and yellow. The like polarized L-band imagery (LVV) is bright, probably because of penetration effects as explained in Section IV. LANDSAT is bright because of the salt crust that covers most of the flood deposits on the salt pan of Death Valley. The purer salts in the flood deposits are lighter than the salts of the massive rock salt unit (Qh). This albedo effect combined with roughness variations allow many details in the salt pan to be seen. In extremely rough terrains, passive reflection data (i.e., visible and near infrared) will be strongly modified by shadowing effects. Except for the special case of imaging at local noon at the solar equator, two effects exist:

(1) Overall decrease in albedo because of shadowing effects.

(2) Spectral shifts generated by the contribution of those areas in shadow that are illuminated by sources having

spectral properties different from direct sunlight (sky, multiple reflections from surface). Evaluation of this effect would involve:

(a) Multiple imaging at different times of day. This option is not possible for rotation-synchronous platforms (e.g., LANDSAT).

(b) Imaging by a sensor that is sensitive to roughness. Knowledge of both the local Sun angle and the surface roughness properties of the surface will permit a semiquantitative albedo correction to be made.

As an example, the surface of the Devil's Golf Course (Qh) consists of steep-sided towers and cavities having local slopes ranging from 45 to 90 deg. The LANDSAT image, acquired at a Sun angle of 48 deg shows Qh as a distinctly darker unit than adjacent Qf (floodplain deposits). Field measurements of shadows for a Sun angle of 50 deg show:

(1) Shadow brightness (estimated from a camera light meter) is less than 10% of the reflectivity of a fully illuminated portion of the silty salt.

(2) Approximately 20% of the surface as seen from above is in shadow.

Taking the albedo of the shadows to be zero, the calculated effect of shadowing is a reduction of the albedo of Qh by 20%. Taking a nominal albedo of 0.5 for silty salt (Neal, 1965) shadowing at 10:00 a.m. reduces Qh's albedo to 0.40. A similar situation occurs on the rough active fans.

In the above situation, the optical sensors can confuse roughness effects with lithology. Information on surface texture derived from multipolarization, multifrequency radar images permit a semiquantitative albedo correction to be made.

Topographic information in the radar imagery creates problems in registration with LANDSAT. Layover is the primary effect that caused problems with the radar imagery used in this report. Illumination angles were nearly the same for the radar imagery and the LANDSAT imagery, which reduced problems due to shadowing.

Imagery obtained at radar and optical wavelengths, though widely separated in the spectrum, can yield useful information when combined. Such a combination of data gathered from Death Valley reveals gravels of different ages, size distribution of rocks near the foot of alluvial fans, and details of evaporite units in the salt pan. The addition of topographic information is subject to geometric distortion effects and, therefore, is of limited use. The fact that radar imagery has a higher resolution (25 m as opposed to 80 m for LANDSAT) adds to the information content of digitally combined radar-LANDSAT imagery.

VI. Digital Image Processing

A. Objective

With the advent of the LANDSAT remote sensing systems and the varied application of imagery from LANDSAT and other orbital and airborne sensors has come the realization of the potential uses of other types of remote sensing data. Systems have begun to appear that invoke a variety of sensing mechanisms to respond to particular target characteristics. While each new sensor is designed to provide information uniquely pertinent to a specific set of applications, the data produced by one system are frequently found to be of interest and value to the user communities of other systems. For this reason the need is becoming increasingly more evident to develop techniques to facilitate and enhance the simultaneous analyses of a multiplicity of data types.

It was precisely such a requirement that prompted the digital processing undertaken to support the analyses of the radar and LANDSAT imagery of Death Valley. The philosophy that underlay the work was to apply the extensive processing capabilities that had already been developed in the Image Processing Laboratory to the particular requirements of an attempt to optimize the simultaneous examination of two types of data. The digital processing procedures that were employed were designed and adjusted to conform to the unique characteristics of radar and LANDSAT imagery. The majority of these techniques, however, are applicable to the general problem of the analyses of multiple types of data of the same target.

B. Facilities

The digital processing was performed using the facilities of the Image Processing Laboratory consisting of a central digital computer, a specialized image processing software system, hardware to convert between photographic imagery and digital sampled arrays, and an interactive processing and display system connected as a satellite of the central computer.

The central computer is an IBM 360/65 using a timesharing operating system with one megabyte of core memory, 900 megabytes of peripheral disk storage, and eight IBM 2400 series tape drives.

The software system, known as VICAR, consists of a high-level command language and a set of application specific

software modules. The system is designed to allow an analyst with little or no familiarity with programming languages to perform a series of digital operations on a sampled image to yield a processed image that may, in turn, be further manipulated or converted to photographic imagery.

Several devices are available to convert between film and digital image arrays. These include two high-speed CRT-based film recorders (one of which can also scan film), a high-resolution drum film recorder, and a high-resolution microdensitometer film scanner.

The interactive system uses a PDP 11/45 to communicate between the central computer, control terminals, and display subsystems. The typical use of the system is to generate single-task VICAR procedures that are fed into the central computer job stream for execution. The product of each step is then further processed or transferred to a display system for observation. Four display systems are available; two 500-line by 500-sample monochrome systems, a 500-line by 500-sample color system, and a 1000-line by 1000-sample monochrome system.

C. Radar Data Generation

Digital radar data were obtained by digitizing image film that had been produced by optically processing raw signal film. The digitization process consisted of recording the amount of light transmitted through the film at a set of locations arranged in an equally spaced rectangular array. The spacing between samples and the area sensed about each sample location were approximately equal. Typical array dimensions for an L-Band image covering the area of one X-band image section were 650 lines by 250 samples. The corresponding X-band sampled array, reflecting the greater resolution of this imagery, contained 3000 lines of 1100 samples.

Because the power in the radar return was more linearly related to film density than to transmission, and because the Image Processing Lab film recording hardware exposes film so as to cause film density to be linearly related to digital sample value, it was necessary to perform an intensity transformation on the digitized data to achieve linearity with film density. The transformation was determined by scanning a photographic wedge of equally spaced density steps at settings identical to those at which the imagery was scanned. The eight-bit digital dynamic range, 0 to 255, was then divided into equal increments, and a piecewise linear transformation was generated that mapped the digitized value of each density step to a unique increment boundary. A plot of a typical scanner correcting intensity transformation is displayed in Fig. 29.

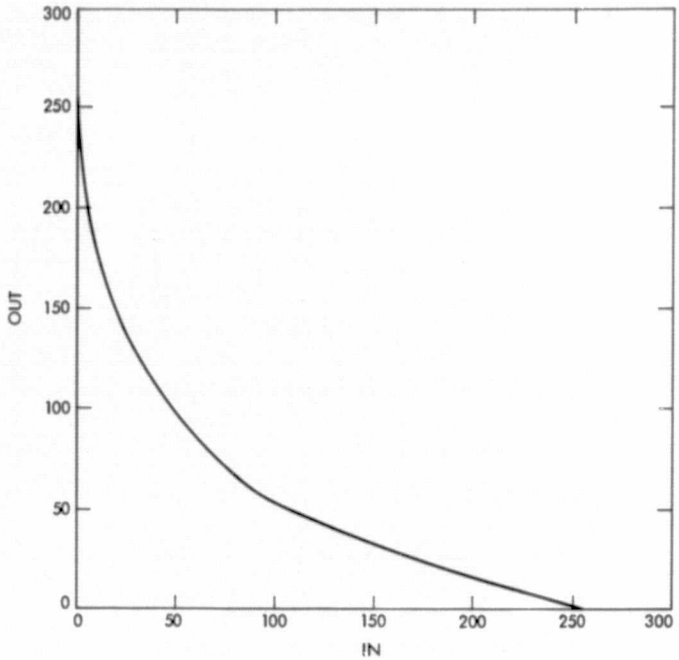

Fig. 29. Scanner correcting intensity transformation

D. LANDSAT Data Preparation

LANDSAT images were obtained from the U.S. Geological Survey in digital sampled form. A LANDSAT scene consisted of four images of the same surface area generated by sensors that responded to different spectral bands of radiation. As received, these data had been only slightly processed to remove sensor characteristics. It was necessary therefore to perform a spatial transformation involving relatively extensive computation to achieve a geometry roughly equivalent to an orthographic projection. The geometric distortions that were addressed in this processing consisted of:

(1) Skew introduced by the rotation of the Earth during recording of the scene

(2) Unequal aspect ratio due to the different sample spacing in the along track and cross track directions

(3) Presence of synthetic image samples that had been introduced to assure the equality of all line lengths

(4) Across-track compression and expansion introduced by variations in the angular velocity of the scanning mirror

(5) Panorama effects that occurred when the pointing vector of the sensor was not perpendicular to the surface

(6) Earth curvature that produced compression at the edges of the imagery

(7) Misregistration between the spectral bands that was produced as a result of the physical configuration of the sensors.

In addition to the geometric corrections, the LANDSAT component images were processed to remove a striping phenomenon that was present in the imagery. This variation in the intensity of successive lines was produced as a result of unequal gains and offsets in the six detectors, each of which sensed every sixth line of the images. The effect was removed by computing histograms of the data from each detector and applying a unique intensity transformation to the data of each detector to cause the six histograms to closely resemble the average histogram.

E. Registration

To perform any of the digital processes that were to simultaneously display or analyze multiple data types, it was first necessary to spatially transform the scenes to bring corresponding surface features to the same location in each image. This registration was accomplished by determining a mathematical relationship that described for each sample location in the master or reference image the location of the corresponding point in the slave image (the image which was to be spatially manipulated to coincide with the master). Ideally, the transformation would have been performed by simply evaluating the mathematical function at each array location in the master image and assigning to that location an estimate of the slave image value at the corresponding location. In practice, computational limitations forced a modification to this procedure that will be described later.

The quality of registration in general depends heavily upon the characteristics of the mathematical relationship that is used. The manual approach, for example, of photographically projecting the images at the same scale and then superimposing them to achieve registration corresponds to assuming the simple mathematical relationship of a translation followed by a linear transformation. If the spatial differences between the two images vary throughout the scene, then this procedure will not produce uniform quality registration over the entire scene. In the case of L-band radar imagery, the compression of the imagery in near range that results from incremental sampling of "line of sight" rather than surface range, is sufficient to render this manual approach inadequate.

The optimal technique is to construct the transformation relationship from mathematical models of all the physical processes that affect the spatial geometry. Given the state of currently available ancillary information for radar data this would constitute an impractical task. Conversion to surface range depends upon topography. To integrate topographic data in the surface range calculation would constitute a major task in itself. The attitude and position of the sensor platform must be very accurately known to correct for their effects. Changes of equipment settings can produce difficult to model discontinuities in the imagery.

Between these extremes lie two approaches that were considered for this project. The more simple of the two consists of assuming a piecewise linear form for the mathematical relationship. In this approach the mathematical function is defined by locating a set of tiepoints (pairs of corresponding points in the two images), and computing the displacement of the slave image from the master image at each tiepoint pair. Displacements at master image locations that fall between the tiepoints are linearly interpolated from those at the surrounding tiepoints. Use of this approach was rejected, however, because a single incorrectly located tiepoint would generate misregistration over a relatively large area surrounding the tiepoint. In addition, extrapolation beyond the area in which tiepoints could be identified would be difficult to perform and would tend to propagate large errors.

The alternative to the piecewise linear technique that was used assumed a polynomial form for the mathematical function relating locations in the two images. The coefficients of the polynomial were determined by "fitting" the polynomial to a set of tiepoints. That is, those coefficients were chosen that minimized the squared distance of the manually located slave image tiepoints from the locations indicated by the polynomial.

In many areas of the scenes, it was difficult to find features that could be precisely located in both images. To identify incorrectly located tiepoints and to evaluate the fidelity with which the computed polynomial modeled the actual spatial variation between the images, the discrepancies (residuals) between the measured tiepoint locations in the slave image and those computed using the polynomial were examined. In addition, the degree of the polynomial was varied, and the residuals were evaluated to determine the polynomial form that best fit the tiepoints.

Ideally, the next step in the procedure would have been to apply the polynomial transformation to each sample location in the master image to obtain the corresponding location in the slave image followed by estimating the slave image value at that location. However, to evaluate the polynomial at as many sample locations as typically existed in the master images (3.3 million points in an X-band scene) would have overtaxed the computational facilities. To reduce the computational load, the polynomial was evaluated only at a sparse grid of control points in the master image. At each of the far more numerous remaining points the corresponding slave image locations were

determined using bilinear interpolation based upon those of four surrounding control points.

The geometrically transformed slave images were generated by assigning to each master image location an estimate of the value of the slave image at the corresponding location. The estimate was obtained from bilinear interpolation between the four neighboring data samples.

F. Color Product Generation

Once sampled arrays of each data type had been generated in which the identical array locations corresponded to the same surface location, it was possible to produce color, difference and ratio imagery to simultaneously display characteristics of several data types.

Color composites of the multiple image types were generated in two ways. The more direct method consisted simply of modulating each of the three primary colors with the image of a single data type. To preclude the domination of the resulting color scene by the component with the greatest average value, all components were subjected to an automated intensity transformation, which forced the distribution of brightnesses in each image to be gaussian with fixed mean and variance. This adjustment had the intended effect of maximizing the color variation in the composite by causing differences between data types to be displayed as hue variations with degrees of difference between each data type producing equal modulation of color saturation and brightness.

A more sophisticated color compositing technique was applied to display imagery of four types simultaneously. In this approach, three spectral bands of LANDSAT imagery were used to supply color information and a radar image to control intensity. To accomplish such a combination, the LANDSAT images were each considered to be a color separation component constituting an independent coordinate of a rectangular three space known as RGB space. A transformation was then performed to a new space, HSI space, defined by a set of coordinates referred to as hue, saturation, and intensity. The HSI space intensity coordinate of a point constituted the distance from the origin along a vector forming equal angles with all R,G,B axes to the intersection with the perpendicular plane containing the point. Qualitatively, the intensity constituted the average brightness of the color point. Hue was defined to be the angle between a vector in the perpendicular plane from the intensity vector to the point and a reference vector in the plane. Thus, the hue coordinate served to differentiate color. The saturation consisted of the angle between the vector from the origin to the point and the gray (zero hue) vector. Saturation, then, described the amount of color.

To combine the LANDSAT and radar data, the radar image was substituted for the intensity image that had been generated by using the LANDSAT data. Color separation images were then obtained by transforming back from HSI space to RGB space.

Because color composites made solely with LANDSAT data had exhibited little color content, even following intensity transformations to increase color, intensity transformations were performed in HSI space on the hue and saturation images. The hue was processed to force a gaussian intensity distribution, and the saturation was increased by multiplication of all values by a constant.

G. Difference and Ratio Product Generation

While difference and ratio images simultaneously displayed only two data types, it was felt that such products would be more easily interpreted than the color composites. Also, the dynamic range of a black-and-white image supporting the display of information from only two data types might more dramatically represent differences than would the dynamic range of a color image supporting information from three types.

Difference and ratio images were generated in a straightforward manner by computing the difference and ratio of corresponding samples of the registered images. To maximize the effect in the difference and ratio images of response variations between the data types, the automated gaussian distribution forcing intensity transformation was executed first. The same transformation was again performed after differencing and ratioing to assure a pleasing visual display. To avoid quantitization problems a multiplication factor was applied during computation of the ratio image.

H. Evaluation of Registration

The approach that was adopted to achieve registration – namely, fitting a polynomial transformation to the observed distortion between sets of corresponding points in two images – has great potential when the processes that produce the distortion are known to generate polynomial dependence. Such is the case, for example, with the proposed NASA system to perform registration of LANDSAT imagery to cartographic coordinate systems. In this system polynomial models of orbital parameters will be fit to sets of corresponding points on maps and LANDSAT images. A subsequent geometric transformation very similar to that employed here is expected to yield registration accurate to within one picture element.

The distortions encountered in radar imagery, however, are not polynomial functions of the picture coordinates. One such

distortion is generated as a result of the incremental sampling of the range from the sensor to the surface rather than the distance on the surface. This system characteristic produces a compression in the image, which increases near the subsensor track on the surface. The function which describes this behavior is not a polynomial:

$$y = [r^2] - [h^2]^{1/2}$$

where y is distance on the surface from the subsensor point, r is distance from the sensor to the surface and h is the height of the sensor above the surface. Besides this specifically nonpolynomial dependence, other mechanisms produce distortions for which mathematical models cannot be generated: the aircraft altitude and surface altitude behave like random variables; the aircraft may turn abruptly; or an operator may change a setting on the instruments within a section of imagery. In view of the nature of both the predictable and unpredictable processes that affect the geometry of radar images, the polynomial fit method of registration can be expected to yield less accurate results when applied to radar imagery than those cited in the LANDSAT example.

The initial attempt to assess registration accuracy consisted simply of examining color products generated from the registered imagery. These products were convenient vehicle with which to check for misregistration, because its presence would produce easily detectable color fringes on abrupt boundaries between bright and dark regions. However, interpretation of any such detected effects need be performed with great care lest real signature variations between the data types be improperly attributed to misregistration.

No such telltale halos were apparent in the color composites of L-band radar and LANDSAT imagery, but under close scrutiny the X-band and L-band color images displayed evidence of misregistration. Further examination on a color CRT display confirmed the existence of a misregistration of approximately five samples in the range direction (across the image) and two samples in the azimuth direction. A surprising result was that the misregistration appeared to exist consistently throughout the entire scene. Because the L-band imagery was lower resolution than the X-band, the registration process caused the L-band to be magnified approximately five times in the vertical direction. In the region of the most obvious misregistration, the horizontal dimension had been expanded by a factor of nearly 10. The inaccuracy, therefore, corresponded to vertical and horizontal errors of one-half sample in terms of the scale of the L-band image.

Because of the small magnitude of the errors in the L-band imagery, it at first seemed reasonable to assume that the misregistration was just the unavoidable consequence of human fallibility locating tiepoints in the L-band images. This convenient explanation was grudgingly forsaken upon the realization that a human being's ability to detect the misregistration implied an equivalent ability to locate points in the L-band image on the average with an accuracy greater than the amount of misregistration. That is, if a person noticed that an edge of a feature in one color did not coincide with the edge in another color, then that person was detecting a series of edge points in one location for one color and in a different location for the other color. When asked to find these edge points in the component images individually the person would, on the average, locate the edges at two different locations in the component images because the same person had already done just that in the color composite.

Based upon this admittedly debatable reasoning a more quantitative investigation was launched. Due to the amount of labor that was to be required for the evaluation, a single test case was chosen – Section 3 of the X-band image. In this case the two L-band images appeared to be relatively well registered to each other. Therefore, only the registration of one L-band image to the X-band image was checked. The evaluation consisted simply of locating pairs of corresponding points in the X-band image and the L-band image that had been geometrically transformed to register with the X-band. Fifty-two points were found in both images, and the magnitudes of the vector errors for all points were computed and averaged. In addition, the horizontal and vertical errors were plotted versus line and sample coordinate in scatter diagrams (Figs. 30, 31, 32, 33), and the average values were calculated.

The quantitative analysis confirmed the existence of the observed misregistration. The average error magnitude was determined to be 6.77 samples, while the average horizontal and vertical errors were 5.19 and 1.60 samples, respectively. The presence of nonzero horizontal and vertical errors was a most disturbing development, because the minimization of

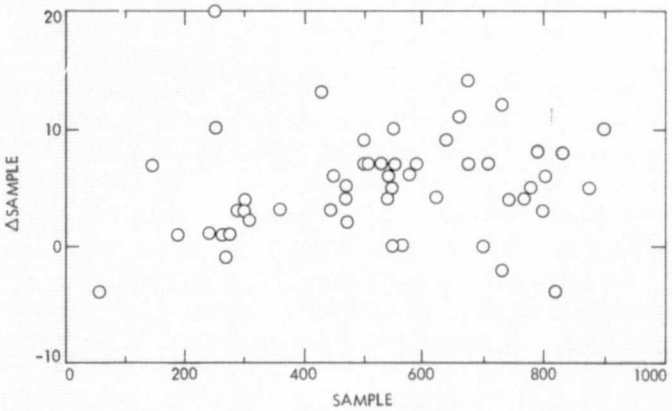

Fig. 30. Horizontal error vs horizontal location

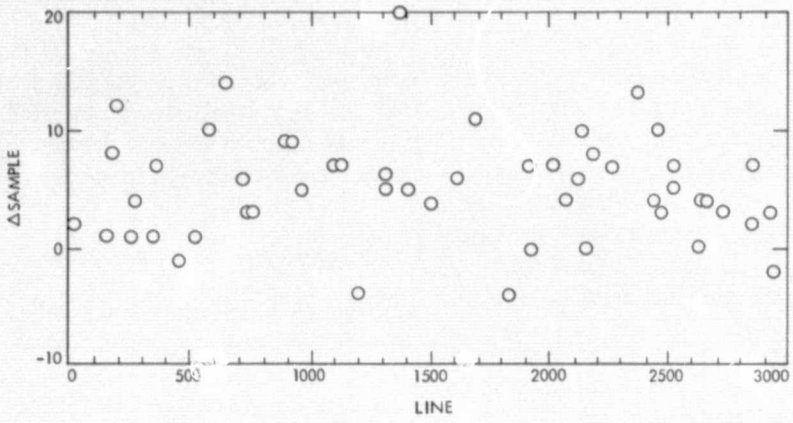

Fig. 31. Horizontal error vs vertical location

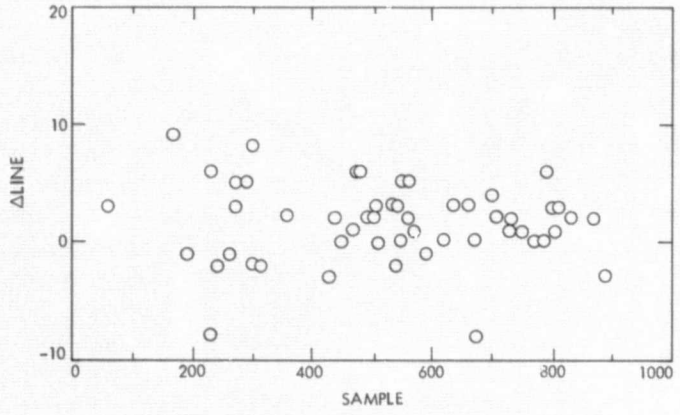

Fig. 32. Vertical error vs horizontal location

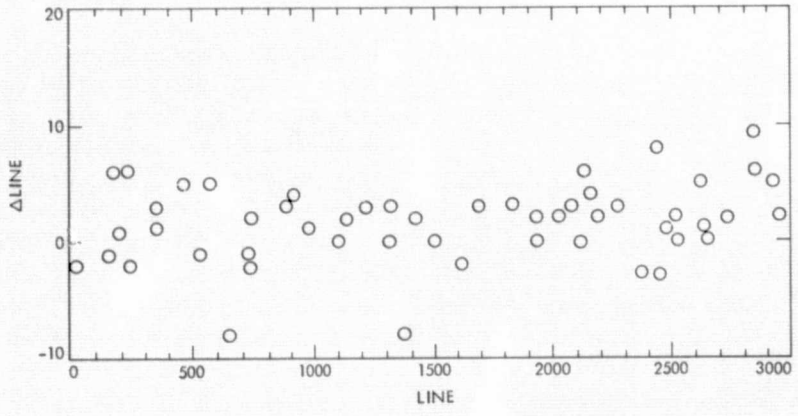

Fig. 33. Vertical error vs vertical location

squared error method of fitting a polynomial theoretically assured average errors of zero.

Another significant conclusion seemed to be relatively well supported by the data; namely, that the errors were consistent over the entire scene. They were not restricted only to local features. Hence, it was decided to be quite unlikely, but not entirely impossible, that the misregistrations were ramifications of signature variations in the two types of sensors. Further support for this opinion was provided in the color composite where both left and right edges of isolated bright or dark features were distorted in the same direction.

At this point a thorough review of the entire registration process was undertaken to determine all potential sources of the errors. Several candidate mechanisms were identified that might have produced the discrepancies. A detailed investigation of the ramifications of each of these on registration accuracy was begun.

As of this writing no specific cause of the error has been isolated. The potentially error producing processes currently under investigation are:

(1) The grid of control points at which the transformation polynomials were evaluated was too sparse, causing the subsequent bilinear interpolation to yield consistently biased errors.

(2) The transformation polynomials were improperly calculated.

(3) Inaccuracies in the magnification of L-band imagery for display at the same scale as the X-band imagery to facilitate the location of tiepoints generated errors that propagated to result in the measured displacements.

(4) The software that performed the geometric transformation and/or that which accomplished magnification computed incorrectly.

(5) Hardware used to determine the location of the tiepoints gave incorrect picture coordinates.

The detailed investigation has been undertaken only on the single frame mentioned. Similar misregistration appears to exist also in Section 4 of the X-band and to L-band color composite. When the source of the errors in Section 3 have been clearly identified, the findings will also apply to Section 4. If it is determined that new products can be generated that will be sufficiently improved to warrant the computational expense and manual effort required, they will be produced. It may also develop that the L-band LANDSAT composites have been adversely affected by the misregistration mechanism. So, new versions of this imagery may also be generated.

In the course of examining the entire set of registered imagery for evidence of misregistration, a local misregistration was detected at the bottom of the color composite generated from LANDSAT and a single L-band imagery. This error was traced to a set of incorrectly located tiepoints in the vicinity of the distortion. To correct this problem, all incorrectly located tiepoints need be relocated and the geometric transformation re-executed with corrected control parameters.

I. Evaluating Color Products

The value of the color composites as well as the ratio images that were generated from the registered imagery lies obviously in the extent to which new information was provided by these products that was not contained in the individual component images. Discussions of the manner in which geologic interpretation and analysis were enhanced by these products are presented in other sections of this report. Some brief comments, however, might be appropriate concerning the degree to which the digital processes were exploited and the ramifications of their characteristics on subsequent analyses.

Subjectively, the color composites appear to utilize a large portion of the available dynamic range. That is, many shades of colors in varying saturation and brightness are present. So, if useful new geologic information has been generated by the color compositing process, it is likely that it is displayed nearly optimally from the standpoint of being detectable.

In addition to providing a display with wide chromatic range, the color products did successfully combine and exhibit information from the individual components in a single image. Comparison of the color composites with the black and white components reveals numerous occurrences of areas of uniform brightness in a single component that exhibit hue, saturation or intensity variation in the color composite.

It should be mentioned that the presence of a wide range of color is partially the result of the application of the automated contrast and brightness adjusting algorithm. In order to achieve a gaussian distribution in the image, this process typically produced a nonlinear transformation of intensity. Since little quantitative use is made of the sample values in the analysis of the color imagery, the fact that a nonlinear transformation was performed is of limited significance. However, a macroscopic characterization of the transformation might be useful. Namely, the typical effect of the algorithm was to move the average brightness to midrange, to increase the contrast about the mean where the most populous brightness occurred, and to reduce the contrast at the brightness extremes at which the least populous brightness were usually found. Plots of examples of these transformations are provided below in the discussion of the ratio products.

J. Difference and Ratio Products

The mathematical process of computing the ratio of two images might be characterized as unstable, in that relatively uninteresting or insignificant differences in the data sets may be dramatically magnified and unduly emphasized. A simple difference in the mean brightness of two images could generate a large average ratio value and cause significant signature variations to produce only small, hence difficult to detect, deviations from the average. Similarly an imbalance in the range of data values in the two images may produce an undesirable domination of the information content of the ratio image by one of the components.

To avoid such difficulties the same automated histogram equalizing transformation employed on the color imagery was applied to the components before computing their ratio. The nonlinearity of this transformation can prove troublesome in subsequent analyses. Therefore, to provide more precise information concerning its effect, plots of typical transformations have been provided (Figs. 34, 35, 36). The plots apply to the same set of images upon which the detailed investigation of registration accuracy was performed.

To assess the value of the digital process from an information theoretic view, it can be noted that a wide range of data values was generated in the ratio picture without incurring large areas of saturation at the brightness extremes. Also, no contouring effects were obvious that would result if only a small band of intensities were occupied by ratio values. The analytic utility of the process was supported by the occurrence, described in the geologic analysis section, of features which appeared to be of relatively similar intensity within each component but which revealed in the ratio image an obvious signature difference.

K. Future Processing

The generation of color composites and ratio images from registered data was useful primarily for qualitative analyses. The new information provided by these products made possible the identification of features or areas of unique image characteristics. Areas discovered in this manner were subsequently checked against geologic maps or field surveys to determine if the uniqueness of their signatures in the imagery implied unique physical properties as well.

A more quantitative approach for extracting information from a multiplicity of data types exists, however. This more sophisticated procedure consists of the application of pattern recognition techniques to identify areas of common image signature. These algorithms offer the primary advantage over color composition and computation of differences and ratios that they can detect unique characteristics simultaneously from many data types rather than only two or three. In addition, surface areas of particular interest can be located in

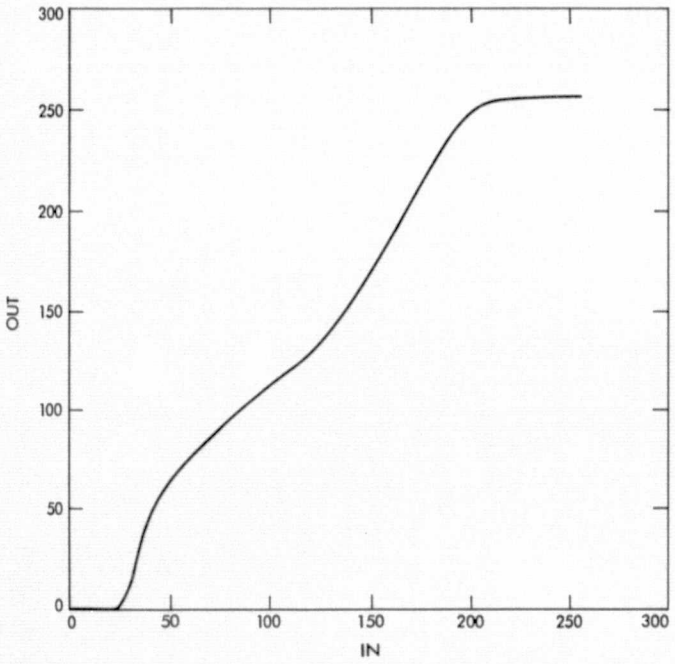

Fig. 34. Intensity transformation to force gaussian distribution in L-band VH

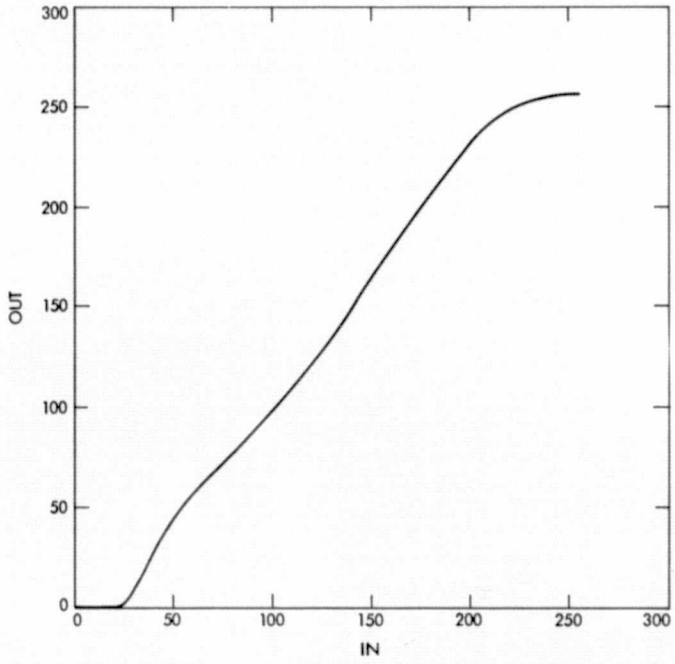

Fig. 35. Intensity transformation to force gaussian distribution in L-band VV

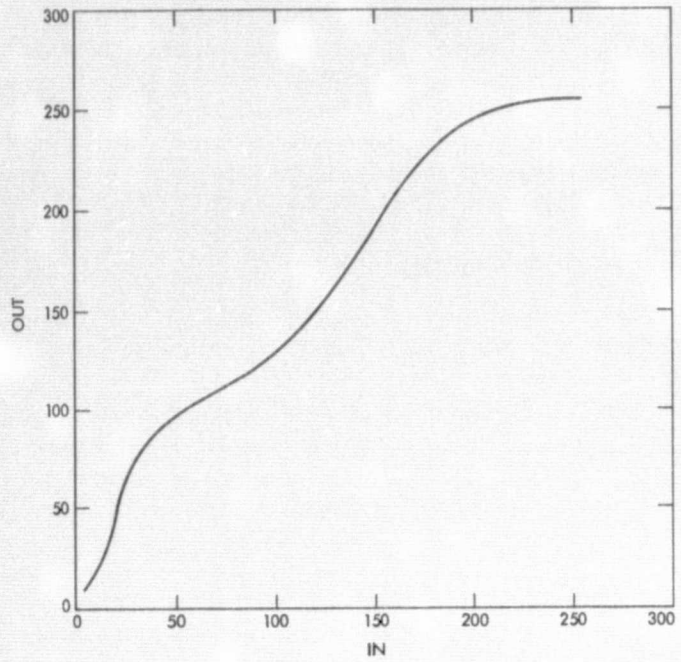

Fig. 36. Intensity transformation to force gaussian distribution in X-band

the imagery and used to "train" automated classifiers. In this way the pattern recognition approach may be invoked to identify all areas of similar signature. Because the pattern classifiers compute based on statistical properties estimated from the data, the validity of the results may be quantitatively assessed, and the processes can be controlled to generate conclusions in specified degrees of confidence.

The software and procedural expertise to pursue this approach have been developed in-house in support of Earth Resources work which has been underway for several years. It is the long-term goal of this project to apply this accessible facility to the data from which the color and ratio products described here have been generated. Specifically, the automated classifications will be carried out in seven-dimensional or higher spaces corresponding to four LANDSAT images, two or more L-band images, and an X-band image. An initial field survey has already been conducted from which ground truth information can be obtained for the initial classification attempt.

Before undertaking the pattern recognition work, however, further registration need be performed and some additional color composite and ratio images will be produced. The required registration consists of achieving correspondence of the X-band radar images with the LANDSAT scene. Completion of this task will allow the generation of an X-band/LANDSAT color composite in which the radar data provide high-resolution intensity information and the LANDSAT data supply color. Various color ratio and difference products are possible using these X-band data, previously registered L-band imagery and the LANDSAT master image.

VII. Geologic Analysis Summary

Precise image registration of several sensor data sets has been achieved by the use of densely populated networks of geometric tiepoints. First-order photometric decalibration of the data sets permitted the generation of ratio and difference images that accentuate subtly different responses between the different sensors.

By using all three radar data sets (direct- and cross-polarized L-band and direct-polarized X-band), a nearly complete discrimination of the lithologic-textural units of Hunt and Mabey (1966) was achieved (Fig. 24). This synergistic effect represents an appreciable improvement in discriminability over any single configuration.

Use of a LANDSAT intensity image provided additional information on varnish distribution on the alluvial fans, thus permitting discrimination of two fan gravel units that were not distinguishable in the radar data. The use of all four bands of LANDSAT should add the capability to distinguish compositions. We thus have seven dimensions of imagery available for computer processing techniques.

Surely, particulate alluvial and colluvial regoliths, evaporites, and eolian deposits represent widespread geologic units on terrestrial planetary surfaces. On cloud covered planets (e.g., Venus), multiconfiguration radar data appears capable of discriminating many of the surficial geologic units likely to exist. On other planets, additional use of optical sensors will permit a more thorough compositional mapping. LANDSAT/radar combinations offer considerable promise for making high-quality geologic maps of lithologic-textural units.

The imaging radar provides first-order information for geomorphologic and topographic mapping. It can be used in a way similar to photography in features identification and classification. The use of multipolarization and multifrequency radar sensors helps in the separation of geologic units where there are subtle differences which are reflected in the surface small-scale topography. The radar sensor can also complement visible and infrared imagers in mapping lithologic units. In areas such as Death Valley, where the lithology has strong impact on the surface roughness, the radar provides first-order information. In other areas where the lithology is mostly reflected in the chemical composition or mineralogical constituents, the radar imagery provides only marginal information.

References

Beckmann, P. (1968), *The depolarization of electromagnetic waves*, The Golden Press, Boulder, Colo.,

Beckmann, P., and Spizzichino, A. M. (1963), *Electromagnetic Scattering from Rough Surfaces*, Pergamon Press, London.

Burns, R. G. (1970), *Mineralogical Applications of Crystal Field Theory*, Cambridge University Press, 224 pp.

Cooper, J. R. (1966), *Radar Imagery of Twin Buttes Area, Arizona Test Site 15*; U.S. Geological Survey Technical Letter, NASA-28, 15 pp.

Daily, M. (1975), *Surface Roughness Discrimination Using L-Band SLAR*, Geological Society of America, Cordilleron Section Abstracts, Annual Meeting, 1975, Pullman, WA.

Dellwig. L. F. (1969), "An Evaluation of Multifrequency Radar Imagery of the Pisgah Crater Area, California," *Modern Geology*, Vol. 1, pp. 65-73.

Denny, C. S. (1965), *Alluvial Fans in the Death Valley Region California and Nevada*, U.S.G.S. Professional Paper 466, 62 pp.

Elachi, C., Roth, L., Kobrick, M., Tiernan, M., and Brown, W. E., "Local Lunar Topography From the Apollo 17 ALSE Radar Imagery," *The Moon*, Vol. 15, pp. 119-131.

Gillerman, E. (1967), *Investigation of Cross-Polarized Radar on Volcanic Rocks*, CRES, Inc., Technical Report 61-25, University of Kansas, 11 pp.

Gillespie, A. R., and Kahle, A. B. (1977), "Construction and Interpretation of a Digital Thermal Inertia Image," *Photogrammetric Engineering and Remote Sensing*, Vol. 43, pp. 983-1000.

Goetz, A. F. H., Billingsley, F. C., Gillespie, A. R., Abrams, M. J., Squires, R. L., Shoemaker, E. M., Lucchitta, I., and Elston, D. P. (1975), *Application of ERTS Images and Image Processing to Regional Geologic Problems and Geologic Mapping in Northern Arizona*, Technical Report 32-1597, Jet Propulsion Laboratory, Pasadena, Calif., May 15, 1975.

Harris, G., and Graham, L. C. (1976), *LANDSAT-Radar Synergism*, paper presented at XIII Congress of the International Society for Photogrammetry, published by Goodyear Aerospace Corp., Litchfield Park, Ariz.

Hooke, R. L. (1967), "Processes on Arid-Region Alluvial Fans," *J. Geology*, Vol. 75, pp. 438-460.

Hunt, C. B., and Mabey, D. R. (1966), *Stratigraphy and Structure, Death Valley, California*, U.S. Geological Survey Professional Paper, 494-A.

Hunt, C. B., Robinson, T. W., Bowles, W. A., and Washburn, A. L., *1966 Hydrologic Basin, Death Valley, Calif.*, U.S. Geological Survey Professional Paper 494-B.

Hunt, G. R., and Salisbury, J. W. (1970), "Visible and Near-Infrared Spectra of Minerals: I. Silicate Minerals," *Modern Geology*, Vol. 1, pp. 283-300.

Hunt, G. R., and Salisbury, J. W. (1971), "Visible and Near-Infrared Spectra of Minerals and Rocks: II. Carbonates," *Modern Geology*, Vol. 2, pp. 23-30.

Hunt, G. R., Salisbury, J. W., and Lenhoff, C. J. (1971), "Visible and Near-Infrared Spectra of Minerals and Rocks: III. Oxides and Hydroxides," *Modern Geology*, Vol. 2, pp. 195-205.

Hunt, G. R., Salisbury, J. W., and Lenhoff, C. J. (1971), "Visible and Near-Infrared Spectra of Minerals and Rocks: IV. Sulphides and Sulphates," *Modern Geology*, Vol. 3, pp. 1-14.

Hunt, G. R., Salisbury, J. W., and Lenhoff, C. J. (1972), "Visible and Near-Infrared Spectra of Minerals and Rocks: V. Halides, Phosphates, Arsenates, Vanadates, and Borates," *Modern Geology*, Vol. 3, pp. 121-132.

Hunt, G. R., Salisbury, J. W., and Lenhoff, C. J. (1973), "Visible and Near-Infrared Spectra of Minerals and Rocks: VI. Additional Silicates," *Modern Geology*, Vol. 4, pp. 85-106.

Hunt, G. R., Salisbury, J. W., and Lenhoff, C. J. (1973), "Visible and Near-Infrared Spectra of Minerals and Rocks: VII. Acidic Igneous Rocks," *Modern Geology*, Vol. 4, pp. 217-224.

Hunt, G. R., and Salisbury, J. W. (1976), "Visible and Near-Infrared Spectra of Minerals and Rocks: XI. Sedimentary Rocks," *Modern Geology*, Vol. 5, pp. 211-217.

Hunt, G. R. and Salisbury, J.W. (1976), "Visible and Near-Infrared Spectra of Minerals and Rock: XII. Metamorphic Rocks," *Modern Geology*, Vol. 5, pp. 219-228.

Hunt, G. R., Salisbury, J. W., and Lenhoff, C. J. (1973), "Visible and Near-Infrared Spectra of Minerals and Rocks: VIII. Intermediate Igneous Rocks," *Modern Geology*, Vol. 4, pp. 237-244.

Hunt, G. R., Salisbury, J. W., and Lenhoff, C. J. (1974), "Visible and Near-Infrared Spectra of Minerals and Rocks: IX. Basic and Ultrabasic Igneous Rocks," *Modern Geology*, Vol. 5, pp. 15-22.

Kahle, A. B. (1977), "A Simple Thermal Model of the Earth's Surface for Geologic Mapping by Remote Sensing," *J. Geophys. Res.* Vol. 82, pp. 1673-1680.

Karr, C. (1975), *Infrared and Raman Spectroscopy of Lunar and Terrestrial Minerals*, Academic Press, New York, 375 pp.

MacDonald, H., and Waite, W. (1973), "Imaging Radars Provide Terrain Texture and Roughness Parameters in Semi-Arid Environments, *Modern Geology*, Vol. 4, pp. 145-158.

McCauley, J. R. (1972), *Surface Configuration as an Explanation for Lithology Related Cross Polarization Radar Image Anomalies*, University of Kansas Center for Research, Inc. Technical Report 177-36, 54 pp.

Matthews, R. E., ed. (1975), *Active Microwave Workshop Report*, NASA SP-376, 502 pp. (Note especially pp. 399-420).

Neal, J. T. (1965), AFCRL-65-266, *Geology, Mineralogy and Hydrology of U.S. Playas*, Air Force Cambridge Research Laboratories, 192 pp.

Noble, L. F., and Wright, L. A. (1954), "Geology of the Central and Southern Death Valley Region, California," in *Geology of Southern California*, California Division of Mines and Geology Bulletin 170, pp. 143-160.

Pollack, J. B., and Whitehill, L. (1972), "A Multiple Scattering Model of the Diffuse Component of Lunar Radar Echoes," *J. of Geophys. Res.*, Vol. 77, p. 4289.

Potter, R. M., and Rossman, G. R. (1977), "Desert Varnish: The Importance of Clay Minerals," *Science*, Vol. 196, pp. 1446-1448.

Potter, R. M., and Rossman, G. R. (1977), "Desert Varnish: Mineralogy of the Ferro-Manganese Oxides," Abstract in *Proceedings of American Geophysical Union*, Fall, 1977 meeting.

Rowan, L. C., Wetlaufer, P. H., Goetz, A. F. H., Billingsley, F. C., and Stewart, J. H (1974), *Discrimination of Rock Types and Detection of Hydrothermally Altered Areas in South-Central Nevada*, U.S. Geological Survey Professional Paper 883, 35 pp.

Ruck, G. T., Barrick, D. E., Stuart, W.D., and Krichbaum, C. K., *Radar Cross Section Handbook*, Plenum Press, New York, 1971.

Schaber, G. C., Berlin, G. L., Brown, W. E., Jr. (1976), "Variations in Surface Roughness Within Death Valley, California: Geologic Evaluation of 25-cm Wavelength Radar Images," *Geol. Soc. Amer. Bull.*, Vol. 87, pp. 29-41.

Smith, H. T. U. (1969), *Photo-interpretation Studies of Desert Basins in Northern Africa*, Air Force Cambridge Research Laboratories, Bedford, Ma.

Valenzuela, G. R. (1967), "Depolarization of EM Waves by Slightly Rough Surfaces," *IEEE Trans. Ant. and Prop.*, AP-15, 552.

Valenzuela, G. R. (1968), "Scattering of Electromagnetic Waves From a Tilted Slightly Rough Surface," *Radio Science*, Vol. 3, pp. 1057-1066.

NASA—JPL—Coml., L.A., Calif.